A dual-scale modelling approach for creep-fatigue crack initiation life prediction of holed structure in a nickel-based superalloy

Kai-Shang Li [a], Lv-Yi Cheng [a], Yilun Xu [b], Run-Zi Wang [a,*], Yong Zhang [a], Xian-Cheng Zhang [a,*], Shan-Tung Tu [a], Hideo Miura [c]

[a] *Key Laboratory of Pressure Systems and Safety, Ministry of Education, East China University of Science and Technology, Shanghai 200237, P.R.China*

[b] *Department of Materials, Imperial College London, SW7 2AZ, UK*

[c] *Fracture and Reliability Research Institute, Graduate School of Engineering, Tohoku University, Sendai, Miyagi 9808579, Japan*

Abstract

In this paper, a dual-scale modelling approach is developed to investigate creep-fatigue behavior and predict crack initiation life for holed structures under multi-axial stress state. The macro-scale simulation supplies local deformation histories to the dual-scale simulation as boundary conditions. In the dual-scale simulation process, the micro-mechanical behavior and damage evolution are described by using crystal plasticity. In order to validate the dual-scale simulation

*Corresponding author: Key Laboratory of Pressure Systems and Safety, Ministry of Education, School of Mechanical and Power Engineering, East China University of Science and Technology, Meilong Road 130, Xuhui District, Shanghai, 200237, P.R. China. Tel.: +86 21 64253513.

E-mail address: rzwang@ecust.edu.cn (R.Z. Wang), xczhang@ecust.edu.cn (X.C. Zhang)

procedures, a series of creep-fatigue tests as well as the post-test characterizations were carried out for nickel-based Inconel 718 at 650 ℃. The detailed results of macro- and micro-scale simulations are presented in terms of stress-strain behavior, damage evolution and life prediction. Regarding the macro-scale simulations as the benchmark, it may provide an assistant support and precognition for the micro-scale damage calculation at higher cycles. The predicted cycle numbers to crack initiation are in agreement with the experimental ones. More advantages are manifested in the potential scientific and engineering significance for the dual-scale modelling approach.

Keywords: Creep-fatigue; Holed specimen; Dual-scale modelling; Crystal plasticity; Life prediction

1 Introduction

Nickel-based superalloys which have outstanding performances at high temperatures are widely used for critical components in aero-engine system, such as compressor aerofoils, shafts and turbine disks. Under such circumstances of unevenly distributed cyclic-thermal-loads, taking off and landing lead to inevitable fatigue damage, and keeping work at a nearly stable temperature results in creep damage in cruise stages [1, 2]. In order to avoid unexpected failure of turbine disks, much attention should be paid on the fatigue damage along with the interaction of creep damage, which is referred to as creep-fatigue [3]. Moreover, considering ventilation and mechanical joint, it is inevitable to introduce geometric discontinuities (i.e., bolted holes, mortises, etc.) into turbine disks. In particular, the distributed bolted

holes are regarded as weak positions to induce the priority failure due to the complicated loading conditions, where fretting fatigue is considered as to be one of the major failure mechanisms [4, 5]. The noticeable stress concentration and severe stress gradient present near the root of bolted holes, resulting in material degradation and facilitating crack initiation. Thus, a reliable life time assessment on the holed structures is necessary to guarantee the safety of parts under in-service conditions.

Different from uniform specimens, the descriptions of cyclic deformation behavior as well as damage evolution for the geometrically discontinuous structures need the supports from finite element method (FEM), which is a robust tool to realize real-time damage estimations [6-8]. In this aspect, reasonable selections for cyclic constitutive model and the corresponding damage model determine the prediction accuracies in deformation behavior and creep-fatigue life. From the perspective of macro-scale, the continuum damage mechanics (CDM) is widely employed in single-factor-driven creep/fatigue damage [9-11], or complicated creep-fatigue interaction [1, 12, 13] due to low computational cost and easy implementation. The fundamental principles of creep-fatigue life prediction are to consider fatigue and creep damages separately, and to subsequently adopt a suitable summation criterion for taking their interactions into account [14]. As for fatigue damage, several models based on critical plane/distance theory were proved to be one of the best-choice methodologies for investigating geometrical discontinuity effect [15, 16]. Nevertheless, researchers found that the energy-based models can provide a more accurate prediction for fatigue life since the effects of local stress and strain fields at the critical positions were considered

simultaneously [17, 18]. As for creep damage, the strain energy density exhaustion (SEDE) models have been argued to be more reliable than stress-based time fraction model [19] or strain-based ductility exhaustion model [20] in multi-axial damage estimations [21, 22]. Although the macro-scale models were in accord with damage assessments and life design requirements, the profound understanding for the microstructure evolution and crack initiation mechanism may not be comprehensively revealed. Therefore, crystal plasticity finite element (CPFE) regarding as an alternative approach was proposed and used in recent decades [23-26]. In such framework, the concept of fatigue indicator parameters (FIPs) was firstly introduced by Manonukul and Dunne [24], and many scholars devoted themselves to applying the proposed FIPs to predict fatigue crack initiation [27, 28]. Among them, the energy-based FIP can reflect the accumulated energy dissipation history and provide more accurate predictability for fatigue life. Adapted from the concept of FIP, various fretting fatigue indicator parameters (FFIPs) have been proposed and applied to predict the fretting fatigue crack initiation life [29-31]. For instance, McCarthy et al. [29] used the accumulated plastic slip to predict the crack initiation life and found the prediction accuracy of the model using crystal plasticity to be superior compared to that using J_2 plasticity. Also, it can further reveal some physical mechanisms for fatigue crack initiation. Wan and Cuddihy et al. [32] found that grain boundaries were the most likely locations for fatigue crack initiation hotpots identified using stored energy criterion. Chen and Dunne et al. [33] revealed that the highest energy-based parameter was closely related to the experimental fatigue crack initiation sites, as

compared to other FIPs. Su et al. [34] found that the equivalent plastic strain was effective for predicting fretting fatigue crack initiation location sits within specimens, which is consistent with the in-situ experimental observations. However, few studies focused on the descriptions of creep damage and the following creep-fatigue life prediction with the aid of the CPFE simulation. In order to address this problem, the accumulated energy dissipation was firstly extended as creep indicator parameter (CIP) to calculate creep damage during hold period. In such a case, the combination of FIP and CIP based on the accumulated energy dissipation was proposed and successfully improved the prediction of creep-fatigue crack initiation life [35]. This work is an extension of Ref. [35] to improve the applicability and the robustness for the life prediction approach.

The traditional representative volume element (RVE) model is no longer suitable for describing local stress and strain gradient fields caused by the geometric discontinuity effect. Even for specimen-level holed structures, the CPFE theory is still difficult to support full-field micro-scale simulation and subsequent analysis due to the considerable increase in computational cost [36]. Thus, with the combinations of the macro- and micro-scale models, dual-scale modelling approach has been developed in some opening literatures [37, 38]. It provides a flexible strategy for the linking the macro-deformation fields with the micro-mechanical response. Herein, several techniques can be applied to bridge the length scales, the respective introductions of which are listed as follows. The methodology of the first modelling technique is to transform the displacement fields of the global model to sub-model as

a boundary condition for the CPFE simulation [39, 40]. The embedded modelling is introduced as the second technique, where the CPFE model is employed at locally weak positions and a simple elastic-plastic model is employed in the matrix outside the micro-scale model [37, 38, 41]. Afterwards, in order to avoid the computational singularity at the interfaces between macro- and micro-scale models, a single crystal FE model was employed in the global matrix instead of the previous elastic-plastic model, which is regarded as the third technique [42]. As discussed above, although dual-scale modelling approaches have been proposed in open literatures [36-42], the specific dual-scale modelling approach has not been implemented in the creep-fatigue context to reveal creep-fatigue crack initiation mechanisms and predict crack initiation life under multi-axial stress state.

In this work, a dual-scale modelling approach is developed to describe the damage evolution and predict the crack initiation life for the holed structures subject to multi-axial stress loading scenario. More specifically, the macro-scale framework with regard to the same object is regarded as a benchmark, enhancing the understanding of the feasibility for the investigated dual-scale FE simulation. The paper is structured as follows. Section 2 introduces the experimental methodology, which includes the early-stage preparations, mechanical tests and post-test examinations. Non-unified (NU) and CP models are two mainstream numerical procedures in this work, as elaborately described in Section 3. The FE modelling description and simulation implementation aiming at the holed structures are given in Section 4. Afterwards, both experimental and simulated results are exhibited in Section 5. Section 6 discusses the

creep-fatigue damage evolutions and life prediction capacities, and Section 7 concludes the main findings of this work.

2 Experimental methodology

2.1 Preparation of specimens

The precipitation-enhanced nickel-based Inconel 718 can maintain its superior mechanical properties at the elevated temperatures. Another characteristic of the superalloy is that the distributions of the three main microstructure phases ($Ni_3(Al, Ti)$ (γ') precipitate, Ni_3Nb (γ'') precipitate and Ni_3Nb (δ) phase) in the γ matrix are particularly sensitive to the heat treatment process. Therefore, the standard heat treatment with the most optimized technological parameters was adopted to the common industrial practice for this material. The detailed steps of the heat treatment contained one-stage solid solution and two-stage aging treatments following the previous works [2, 35], as schematically shown in Fig. 1.

The uniaxial round bar specimens with the gauge-length of 30 mm and the diameter of 8 mm were tested on the MTS model 809 A/T testing system to obtain the fundamental fatigue and creep-fatigue properties. The central circular hole specimens with thickness of 4 mm and hole diameter of 10 mm were selected to imitate actual bolt holes in turbine disks. The geometric shapes and dimensions of both specimens are shown in Table 1. The gauge sections of all uniaxial and holed specimens were finely polished up to remove the machining residual stress.

2.2 Creep-fatigue tests

A series of creep-fatigue tests were carried out at 650 ℃ for the specimens with and

without a central hole. The selected temperature was considered as an upper-limited in-service temperature for the turbine disks made by Inconel 718 as the strengthening γ" precipitation heavily transforms to the equilibrium δ phase at that temperature. Considering the severe degradation in mechanical performance of the alloy above 650 ℃, it was of great indicative significance to predict the creep-fatigue life for the material at the investigated temperature of 650 ℃. The detailed parameters in creep-fatigue tests for Inconel 718 are summarized in Table 1. Specimens U1 to U10 represented uniaxial specimens and specimens H1 to H8 were holed specimens, all of which were subjected to global strain-controlled mode within the gauge section, as shown in Fig. 2. Specimens U1 to U10 were used to calibrate the material parameters in NU and CP constitutive models, while specimens H1 to H8 were used to explore the creep-fatigue behavior under multi-scale stress state with the aid of the dual-scale modelling approach. The trapezoidal loading waveforms were selected for the creep-fatigue tests with a unified strain ratio, R_ε=0. For holed specimens, the total strain ranges, $\Delta\varepsilon_t$, were selected to be 0.3% and 0.4% and hold times, t_h, under each $\Delta\varepsilon_t$ were selected to be 0 s, 60 s, 300 s and 1800 s, as listed in Table 1. In order to monitor and control the global axial strain, two ceramic rods of the high-temperature extensometer were symmetrically attached onto the gauge section of each specimen, which was heated by a MTS model 653 high-temperature furnace, as shown in Fig. 2. The nominal temperature of this furnace ranges from 100 ℃ to 1400 ℃ and the control point stability was roughly ±1 ℃. The high-temperature furnace and temperature monitor in the temperature measurement system were used to monitor

and control the temperature field during creep-fatigue tests, respectively. Clamping heads were equipped with a water-cooling system to prevent overheating and ensure the stability of the clamping force. Prior to the tests, the operation system and temperature measurement system were calibrated to ensure the validity and accuracy of high-temperature tests.

2.3 Microstructure characterization

Prior to creep-fatigue tests, a cubic-shaped sample (4 mm × 4 mm × 4 mm) was extracted from the heat treated material to obtain initial microstructure using electron backscatter diffraction (EBSD). Subsequently, the fracture appearances were observed by scanning electron microscope (SEM) to identify hold time effect on crack initiation mechanisms by comparing specimens H5 ($\Delta\varepsilon_t$=0.4 %, t_h=0 s) and H8 ($\Delta\varepsilon_t$=0.4 %, t_h=1800 s). Moreover, the post-test EBSD characterization was conducted to analyze the creep-fatigue damage mechanism near to the holed root for specimen H8. The surfaces of extracted EBSD specimens were mechanically ground up a mirror surface and then were electrochemically polished in a mixture composition of 90% Ethanol and 10% Perchloric acid at -25 °C. CamScan Apollo 300 scanning electron microscopy equipped with Hikari detector was used to capture the Kikuchi patterns with a fixed scanning step of 0.8 μm.

3 Numerical procedures

3.1 Overview of numerical procedures

The overall flow chart of the dual-scale modelling approach for creep-fatigue life prediction of the holed structures is shown in Fig. 3. Different constitutive models and

FE models at the corresponding macro- and micro-scale play different roles in the dual-scale modelling approach. The constitutive models with the combinations of NU and CP models are used to describe the stress-strain responses resulting from the intrinsic performance of the material. The FE models include the RVE model for calibrating constitutive model parameters and holed structure FE model for simulating creep-fatigue behavior. Firstly, the macro-scale framework is regarded as the precondition and benchmark for investigating the damage mechanism and life prediction. In this framework, a NU constitutive model is implemented via the finite element code ABAQUS using user subroutine, where the macro-scale RVE model is established to determine the NU model parameters from a calibration process stated in section 5.1.1. Afterwards, the FE model of the holed specimens is constructed to simulate the creep-fatigue behavior, during which the real-time stress and strain fields were extracted to calculate the damage given by fatigue and creep in the energy-based damage model. Secondly, the micro-scale framework is used to reveal the crack initiation mechanisms and predict the crack initiation life for the holed specimens. In this framework, the CP constitutive model was integrated into a user material subroutine (umat), and the model parameters was calibrated by implementing the RVE simulation based on trial-and-error method. The displacement field of macro-scale FE model is passed as boundary conditions to impose on the CPFE model at the holed root. Afterwards, the accumulated energy dissipation is extracted to calculate the critical FIP and CIP. Finally, with the help of linear damage summation (LDS) rule, if the summation of accumulated fatigue and creep damages equals to 1 at the most

dangerous position, the final creep-fatigue crack initiation life can be determined.

In summary, the NU model is designed as a benchmark to support the dual-scale system for the holed structures, while CP model is used to reveal the creep-fatigue damage mechanisms at holed root by the combination of microstructure and local stress concentration. The constitutive formulations of models at both macro- and micro-scales will be introduced in the following sections.

3.2 Theory based on viscoplasticity

3.2.1 NU model

The aims of NU model are to depict the macro-mechanical responses for the holed specimens and to explore as the benchmark for the dual-scale FE simulation. The main formulations of the NU model are written as follows [43, 44],

$$\dot{\varepsilon} = \dot{\varepsilon}^e + \dot{\varepsilon}^p + \dot{\varepsilon}^c \tag{1}$$

where the total strain rate, $\dot{\varepsilon}$, is separated into the elastic component, $\dot{\varepsilon}^e$, the plastic component, $\dot{\varepsilon}^p$, and the creep component, $\dot{\varepsilon}^c$, which are respectively written as,

$$\dot{\varepsilon}^e = \mathbf{D}^{-1} : \dot{\sigma} \tag{2}$$

$$\dot{\varepsilon}^p = \dot{\lambda} \frac{\partial f}{\partial \sigma} \tag{3}$$

$$\dot{\varepsilon}^c = \left[\psi \tilde{q}^n \left(\varepsilon^c \right)^m \left(m+1 \right)^m \right]^{1/(m+1)} \tag{4}$$

where, $\mathbf{D}$ is the fourth-order Hook elastic tensor. and $\dot{\sigma}$ is the Cauchy stress rate tensor. $\dot{\lambda}$ is the plastic multiplier satisfying the consistency condition of yield function $f = \dot{f} = 0$. $\tilde{q}$ is the equivalent deviatoric stress, and ψ, m and n are material parameters depending on temperature. Following Eq. (3), the yield function can be expressed as,

$$f=\left[\frac{3}{2}\left(\sigma'-\chi'\right):\left(\sigma'-\chi'\right)\right]^{1/2}-Q_0-R \tag{5}$$

where σ' and χ' are the deviators of stress tensor and back stress tensor, respectively. Q_0 is the initial yield stress and R is the isotropic deformation resistance. The equation of $\dot{\chi}$ in NU model can be written as,

$$\dot{\chi}^{(l)}=\frac{2}{3}\zeta^{(l)}r^{(l)}\dot{\varepsilon}^{p}-\zeta^{(l)}\chi^{(l)}\dot{p} \tag{6}$$

where the index l (l=1, 2, 3) indicates that $\dot{\chi}$ is decomposed into three parts to illustrate the nonlinearity during plasticity. $\zeta^{(l)}$ and $r^{(l)}$ are the material parameters. $\dot{p}=\sqrt{\frac{2}{3}\dot{\varepsilon}^{p}:\dot{\varepsilon}^{p}}$ is the accumulated equivalent plastic strain rate. The isotropic deformation resistance rate, $\dot{R}$ can be expressed as,

$$\dot{R}=b\left(R_{sat}-R\right)\dot{p} \tag{7}$$

where R_{sat} is the saturated value of isotropic deformation resistance and b is the speed that approaches to the saturated value of R_{sat}. It is noted that the rate-independent plasticity and the rate-dependent creep are considered separately in the NU model to coupe with creep-fatigue stress-strain response. There are several reasons for applying the constitutive model in this work. Firstly, as compared to the unified viscoplasticity model, the NU one is easier implementation and less computational expense. Secondly, the variations of strain rate have limited influence on fatigue and creep-fatigue life in nickel-based alloy at 650 ℃ [45]. This indicates that the rate-independent plasticity is almost independent on creep-fatigue endurances, which is regarded as the main disadvantage of NU model [46]. Hence the rate sensitivity effect can be neglected. In addition, the effect of hold time has little

influence on the experimental cyclic softening curves, which is a universal observation for the alloy [45, 47, 48].

3.2.2 Calculations of creep and fatigue damage at macro-scale

The SEDE criterion in the macro-scale framework has been employed to evaluate the creep-fatigue damage and predict crack initiation life under both uniaxial [49, 50] and multi-axial states [2, 51]. In this paper, an energy-based model is developed to predict the creep-fatigue crack initiation life for the holed specimens, including separated fatigue and creep damage formulations. Although one single temperature is considered only, the application of the life prediction model can further extended by recalibrating the temperature-dependent material parameters.

Ellyin and Golos [52] firstly introduced the strain energy density to describe the fatigue, which is written as follows,

$$\Delta w_{tot} = \Delta w_{el} + \Delta w_{pl} \tag{8}$$

where Δw_{tot} is the total strain energy density per cycle. Δw_{el} and Δw_{pl} are respectively the elastic and plastic strain energy density per cycle, schematically represented in Fig. 4a as the shaded area. The fatigue damage per cycle, $d_{f,macro}$, is expressed as,

$$d_{f,macro} = \frac{1}{m_f \left(\Delta w_{tot}\right)^{-n_f}} \tag{9}$$

where m_f and n_f are two material parameters.

In our previous work [2], the multi-axial creep damage was accurately calculated by the dominated parameters of creep strain energy density rate and failure strain energy density with taking elastic follow-up factor into account. Although the SEDE

approach takes the advantage in fulfilling the high accurate prediction capabilities, the equation in integral form is difficult to be extended to engineering application, i.e.,

$$d_{c,macro} = \int_0^{t_h} \left[\frac{\dot{w}_c}{\min\left(w_f, w_{f,crit}\right)} - \frac{\dot{w}_c}{w_{f,crit}} \right] dt \tag{10}$$

where $d_{c,macro}$ is creep damage per cycle. $\dot{w}_c$ is the creep strain energy density rate and w_f is the failure strain energy density per cycle. $w_{f,crit}$ is the critical strain energy density, which is of significance to describe creep-free phenomenon at extremely short hold times. In order to reduce computational expense and improve applicability, Eq. (10) is simplified to be a discrete form that is easy to be applied to engineering problems.

$$d_{c,macro} = \sum_{i=1}^{k} d_c^{(i)} = \sum_{i=1}^{k} \left[\frac{\dot{w}_c^{(i)}}{\min\left(w_f^{(i)}, w_{f,crit}\right)} - \frac{\dot{w}_c^{(i)}}{w_{f,crit}} \right] \tag{11}$$

where,

$$\dot{w}_c^{(i)} = \frac{\left(\bar{\sigma}_0^{(i)} - \bar{\sigma}_m\right) \cdot \varepsilon_c^{(i)}}{\tau^{(i)}} \tag{12a}$$

$$w_f^{(i)} = m_c \left[\dot{w}_c^{(i)} \right]^{n_c} \tag{12b}$$

where the index *i* indicates the number of incremental steps that increases to *k* per cycle at FE simulation. $\dot{w}_c^{(i)}$ is the creep strain energy density rate at an incremental step. $\bar{\sigma}_0^{(i)}$ is the equivalent peak tensile stress at an incremental step. $\bar{\sigma}_m$ is the equivalent mean stress per cycle, as shown in Fig. 4b. m_c and n_c are two material parameters in Eq. (12b).

3.3 Theory based on CP

3.3.1 CP model

CP model can be used to illustrate the local response within individual grains and the interaction among neighboring grains. In the present work, a rate-dependent formulations in CP model proposed by Busso [53] and Li et al. [54] were selected to analyze the creep-fatigue behavior of Inconel 718. In addition, other microstructural details such as precipitates [55, 56] may play an important role in creep-fatigue damage. The microstructural response acts as stress concentration, leading to localized energy dissipation in the vicinity of precipitates that would possibly suspicious sites for crack initiation. Due to the strong coherency between the precipitate phases and the matrix [55], they are homogenized as a RVE to represent the mechanical properties of Inconel 718 at the micro-scale. An disadvantage of the method should be mentioned that the effects precipitates γ' and γ'' cannot be investigated explicitly. Therefore, in future work, a dual-scale modelling from micro to nano-scale would be developed to investigate the precipitate effect on creep-fatigue behavior. The kinetics of crystal deformation is expressed by a decomposition of deformation gradient, $\mathbf{F}$, into elastic and plastic deformation gradients, $\mathbf{F}^e$ and $\mathbf{F}^p$, i.e.,

$$\mathbf{F} = \mathbf{F}^e \cdot \mathbf{F}^p \tag{13}$$

The plastic velocity gradient, $\mathbf{L}^p$, can be represented by plastic deformation gradient as follows,

$$\mathbf{L}^p = \dot{\mathbf{F}}^p \mathbf{F}^{p-1} = \sum_{\alpha=1}^{n} \dot{\gamma}^\alpha \mathbf{s}^\alpha \otimes \mathbf{m}^\alpha \tag{14}$$

where n=12 indicates the number of slip systems. $\mathbf{s}^\alpha$ and $\mathbf{m}^\alpha$ represent the slip direction and slip plane normal of the αth slip system. $\dot{\gamma}^\alpha$ is the crystal plastic slip

rate on the αth slip system, which can be described by a thermally activated flow rule containing two state variables of slip resistance, S^{α}, and back stress, B^{α}, on the αth slip system, i.e.,

$$\dot{\gamma}^{\alpha}=\dot{\gamma}_0\exp\left[-\frac{F_0}{k\theta}\left\langle 1-\left\langle\frac{\left|\tau^{\alpha}-B^{\alpha}\right|-S^{\alpha}}{\tau_0}\right\rangle^{p}\right\rangle^{q}\right]\operatorname{sgn}\left(\tau^{\alpha}-B^{\alpha}\right) \tag{15}$$

where $\dot{\gamma}_0$ is the reference strain rate. k is the Boltzmann constant. θ is the absolute temperature. F_0 is total free energy for a dislocation required to overcome the lattice resistance. τ_0 is the lattice friction stress at the current temperature. p and q are two exponential constants related to material properties. The resolved shear stress on the αth slip system, τ^{α} is written as [57],

$$\tau^{\alpha}=\mathbf{F}^{e\mathrm{T}}\mathbf{F}^{e}\mathbf{T}^{*}:\left(\mathbf{s}^{\alpha}\otimes\mathbf{m}^{\alpha}\right) \tag{16}$$

$$\mathbf{T}^{*}=\zeta:\mathbf{E}^{e} \tag{17}$$

where $\mathbf{T}^{*}$ represents the second Piola-Kirchoff stress, $\mathbf{E}^{e}$ is elastic Green tensor, and ζ is elastic stiffness tensor. The slip resistance, S^{α}, is defined as,

$$\dot{S}^{\alpha}=\sum_{\beta=1}^{n}h^{\alpha\beta}\left(\frac{S_{sat}-S^{\beta}}{S_{sat}-S_0}\right)\left|\dot{\gamma}^{\beta}\right| \tag{18}$$

$$h^{\alpha\beta}=h_s\left[w+\left(1-w\right)\delta^{\alpha\beta}\right] \tag{19}$$

where S_0 and S_{sat} are the initial and saturated resistance. $h^{\alpha\beta}$ is the hardening matrix which is used to describe the cross-hardening behavior between the slip systems α and β. h_s is the material constants. w is the latent hardening ratio and $\delta^{\alpha\beta}$ is the Kronecker delta. The back stress, B^{α}, is set as [35],

$$\dot{B}^{\alpha}=h_B\dot{\gamma}^{\alpha}-\frac{r_D}{S^{\alpha}}B^{\alpha}\left|\dot{\gamma}^{\alpha}\right|+r_S B^{\alpha} \tag{20}$$

where h_B is the hardening constant. r_D is the dynamic recovery parameter and r_S is the

static recovery parameter.

3.3.2 Calculations of creep and fatigue damage at micro-scale

Based on the CPFE simulation, the fatigue life prediction is carried out by using FIPs, such as statistical standard deviation of strains [58], accumulated plastic slip [24, 27] and accumulated energy dissipation [59, 60]. Among these FIPs, the physical-based energy dissipation, W, can fulfil a highly accurate prediction for the number of fatigue cycles, which is written as

$$W = \sum_{\alpha=1}^{n} \int_0^t \tau^\alpha \dot{\gamma}^\alpha dt \tag{21}$$

It is deemed that fatigue crack initiation occurs when the critical accumulated energy dissipation, W_{crit}, is achieved. Afterwards, in order to predict the creep-fatigue life, the FIP is extended to creep-fatigue damage description in our previous work [35], where the accumulated energy dissipation is decomposed into two parts to respectively describe the degrees of creep and fatigue damages. The energy dissipation accumulated from hold-begin to hold-end points is designated as CIP to express creep damage, while the physical-based parameter extracted during loading/unloading period is considered as FIP to describe fatigue damage. In this approach, the fatigue damage per cycle, $d_{f,micro}$, is defined as

$$d_{f,micro} = \frac{W_{f,\text{cyc}}}{W_{f,\text{crit}}} \tag{23}$$

where $W_{f,\text{crit}}$ is the critical FIP and $W_{f,\text{cyc}}$ is the FIP per cycle. The creep damage accumulated per cycle, $d_{c,micro}$ is summated as

$$d_{c,micro}=\int_0^{t_h}\left(\frac{\dot{W}_{c,\mathrm{cyc}}}{W_{c,\mathrm{crit}}}\right)dt \tag{24}$$

where $W_{c,\mathrm{crit}}$ is the critical CIP and $\dot{W}_{c,\mathrm{cyc}}$ is the energy dissipation rate during the hold time per cycle.

4 FE modelling implementations

4.1 Macro-scale FE modelling strategies

Two macro-scale FE models for uniaxial and holed specimens were respectively established by using the commercial software ABAQUS. As shown in Fig. 5a, the macro-scale RVE model for the uniaxial specimens was used to calibrate and validate NU model parameters. Considering the reasonable computational consumption, a symmetrical FE model in gauge section for the holed specimens was simplified as a two-dimensional symmetric problem so as to implement the creep-fatigue simulations, as seen in Fig. 5b. A 4-node bilinear plane strain quadrilateral (CPE4) element was used in the FE model and each element size at the holed root was approximately 0.1 mm × 0.1 mm, while the mesh size away from the holed root was much coarser as shown in Fig. 5b. The symmetry boundary conditions were employed on the left sides. The fixed constraint in *y*-direction was employed on the bottom side. The displacement was applied in *y*-direction to simulate creep-fatigue cyclic loadings at the reference point (RP) above the top side.

4.2 Micro-scale RVE modelling strategies for uniaxial specimens

To calibrate and validate the CP model parameters, a micro-scale RVE model is constructed according to the two requirements: (i) whether it can reflect the crystal anisotropy at micro-scale; (ii) whether the model can represent uniform mechanical

properties at macro-scale. In this work, the Voronoi Tessellation technique was used to generate the micro-scale RVE model with uniform crystalline morphology and randomly distributed grain orientation for the investigated material. The average grain size was approximately 20 μm, as embedded in Fig. 1. As shown in Fig. 6a, a plane-strain microstructure-based RVE model consisting 300 grains was used to duplicate the hysteresis loops. The configurations of boundary conditions and loading direction for the micro-scale RVE model were also illustrated in Fig. 6a. All the nodes on the bottom side were constrained in *y*-direction. The multi-point constraints represented by small black circles were implemented to all the nodes on the left and right sides so that they were enforced to move in the same *x*-direction. The constraint method can accurately predict the mechanical behavior with a certain number of grains in the micro-scale RVE model [28, 61]. The *y*-direction displacement loading at RP in Fig. 6a was applied to all nodes on the top side. The micro-scale RVE model was used to calibrate the CP model parameters for further simulating the creep-fatigue behavior of holed specimens.

4.3 Dual-scale modelling strategies for holed specimens

Due to the enormous computational cost, it is difficult to use the specimen-level model constructed by millions of grains to achieve the CPFE simulation of the holed specimens. Therefore, the dual-scale modelling approach is used in this work as shown in Fig. 6b. The objective of the modelling approach was to transmit the displacement field of macro-scale FE model constructed in section 4.1 to the sub-model (CPFE model in Fig. 6b) as boundary conditions, as mentioned in section

3.1. It is well acknowledged the crack always initiates at the holed root under cyclic loading conditions, while the area that is not subject to obvious plastic deformation is regarded as the far-field region [37, 62]. Under this circumstance, the detailed procedures of the dual-scale modelling are displayed in Fig. 6b. Firstly, the NU model was calculated by macro-scale FE model to simulate the creep-fatigue response of the holed specimens. Secondly, the nodal displacements at the interesting region were extracted and applied to each boundary node in the sub-model. Finally, the investigation of the creep-fatigue behavior at the holed root was likely to be achieved with no need for simulating a large number of microstructures. That was to say, in the macro-scale simulation, the deformation behavior of Inconel 718 under creep-fatigue loading conditions was investigated using the phenomenological NU model. The micro-scale CPFE simulation provided the local microstructure evolution and accumulated energy dissipation at holed root for revealing the damage mechanism and predicting the crack initiation life. Therefore, the dual-scale referred to that the spatial scale varies from macroscopic deformation at the NU model to microstructure deformation at the CP model.

5 Results

5.1 Identification of the material parameters

5.1.1 Calibration of NU model parameters

The uniaxial specimens (listed in Table 1) are investigated to determine the constitutive model parameters and energy-based damage variables at macro-scale, which can be carefully classified into five categories: (I) basic material constants, (II)

non-linear kinematic hardening parameters, (III) strain-hardening creep parameters, (IV) isotropic hardening parameters, and (V) creep-fatigue damage parameters. It should be mentioned that the material parameters in categories II and III are independently determined because of that the plastic-cyclic behavior and the stress-relaxation behavior (equivalent to creep behavior) do not give a coupling effect in the UN constitutive model. Based on the effect of the above-mentioned parameters on the cyclic softening behavior, the isotropic hardening parameters in category IV are finally determined. As illustrated in Fig. 7a, the determination procedure is detailed as follows: (1) all the parameters are classified according to their properties as mentioned above; (2) the basic material parameters of E, v and Q_0 in category I are determined by using the monotonic tensile curve in Inconel 718 at 650 ℃; (3) the strain-stress experimental data during the first cycle are used to estimate the non-linear kinematic hardening parameters of $\xi^{(i)}$ and $r^{(i)}$ following the procedures suggested Kang et al. [63]; (4) the strain-hardening creep parameters of ψ, m and n are determined through the stress relaxation experimental data in the first cycle; (5) the cyclic stress response curve is used to estimate the isotropic hardening parameters of R_{sat} and b [64]; (6) the damage parameters of m_f and n_f are determined by fitting the relation of fatigue crack initiation life N_i vs. total strain energy density Δw_{tot} extracted from the five pure fatigue experimental results (see Fig. 8), while the damage parameters of m_c and n_c are determined by comparing the critical strain energy density w_f vs. the creep strain energy density rate $\dot{w}_c$ obtained from pure creep data [65]. By using the aforementioned step-by-step procedures, the material parameters in the NU

model and energy-based damage model are identified and listed in Table 2.

5.1.2 Calibration of CP model parameters

A uniaxial specimen of U7 ($\Delta\varepsilon_t$=1.6%, t_h=1800s) is selected to calibrate the CP model parameters, which are classified into four categories: (I) anisotropic stiffness constants, (II) flow parameters, (III) hardening parameters and (IV) creep-fatigue indicator parameters. The step-by-step calibration procedure is shown in Fig. 7b. In the first step, all the CP model parameters are classified into four categories as mentioned above. In the second step, the anisotropic stiffness constants are first evaluated by simulating the elastic response of the RVE model subjected to monotonic tensile loading. In the third step, some common parameters of γ_0, F_0 and w are directly determined from the literatures about nickel-based superalloys [66, 67]. In the fourth step, the flow parameters of p, q and τ_0 are determined by fitting tensile curve by using trial-and-error method. In the fifth step, the kinematic hardening parameters of h_B, r_D, r_S and isotropic hardening parameters of h_B, r_D, r_S are identified by calculations of cyclic loading to simulate the experimental hysteresis loop and stress relaxation curve for the selected specimen. All CP model parameters are listed in Table 3. In the final step, the two critical values of FIP and CIP ($W_{f,\mathrm{crit}}$ and $W_{c,\mathrm{crit}}$) in Eq. (23) and Eq. (24) are identified to predict creep-fatigue crack initiation life. It has been clarified that $W_{f,\mathrm{crit}}$ is independent of the loading conditions [28, 35, 68], and the independence of $W_{c,\mathrm{crit}}$ has been also explored in our previous study [35]. Therefore, the fundamental parameters $W_{f,\mathrm{crit}}$ and $W_{c,\mathrm{crit}}$ were respectively determined by multiplying the selected experimental crack initiation life N_i by the simulated values

of $W_{f,\mathrm{cyc}}$ and $W_{c,\mathrm{cyc}}$ at a stabilized cycle.

5.2 Validation of the parameters in both numerical models

The material parameters in NU and CP models were validated in terms of the hysteresis loops and stress relaxation curves of the specimens U3, U6 and U10 with t_h=300s. The comparison between the experimental hysteresis loops and the numerical ones in terms of the first cycle are shown in Figs. 9a-c, presenting a good match between both results. Due to the creep embrittlement property of the nickel-based superalloy [69], the relaxed stress magnitude during the hold time period is difficult to be observed in the hysteresis loops. Thus the experimental and simulated stress relaxation curves were plotted in Figs. 9d-f. The experimental relaxation curves are in agreement with the simulated results obtained from NU and CP models. In addition, the maximum error between the experimental and simulated stress is used to analyze the accuracy of NU and CP predictions. The error formula is given as follows,

$$\mathrm{Error}=\left|\frac{\sigma_{\mathrm{exp}}-\sigma_{\mathrm{sim}}}{\sigma_{\mathrm{exp}}}\right| \tag{25}$$

where σ_{exp} and σ_{sim} are the experimental and simulated stress. The values of σ_{exp} and σ_{sim} are selected when their discrepancy in hysteresis loops or stress relaxation curves are the largest at a given strain. All the maximum errors in hysteresis hoops are less than 10% and in the stress relaxation curves are less than 2% (see Fig. 9g-i). The comparisons in Figs. 9a-f and the maximum error analysis in Figs. 9g-i suggest that the calibrated material parameters of both constitutive models are reasonably representative for further investigations.

5.3 Sensitivity studies in CPFE simulation

5.3.1 Mesh sensitivity analysis

Before conducting the CPFE simulation, the sensitivity studies were adopted to exclude the mesh and microstructure effects on damage evolution and life prediction with the help of the tensile curve at 650 ℃. The mesh sizes of the corresponding micro-scale RVE models were set to be 0.001 mm, 0.002 mm and 0.003 mm. A small gap between the simulated curve with coarse mesh (0.003 mm) and experimental tensile curve was observed in Fig. 10a. However, the simulated curves with medium mesh (0.002 mm) and fine mesh (0.001 mm) were well agreed with the experimental data. In addition, the accumulated energy dissipation bands in the RVE models with fine and medium meshes were more obvious than those with coarse mesh. The significant locations with maximum accumulated energy dissipation were detected from the RVE models with fine and medium meshes, but disappeared from that with the coarse mesh, see Fig. 10a. Herein, the medium mesh was enough for the subsequent CPFE simulation when the computational cost was considered in the numerical process. Based on this, the selected medium mesh was used to conduct the microstructure effect on CPFE analysis, involving grain structures and orientations. Figure 10b gives the comparison between the experimental tensile curves and simulated results with three microstructures named as M1, M2 and M3. The CPFE simulated curves by adopting the corresponding microstructures were almost identical with the experimental results, as seen in Fig. 10b. Furthermore, all the energy dissipation fields presented a common localization pattern that significant local

energy dissipation bands formed about 45° relative to the loading direction. Therefore, the effect of microstructure distribution on the CPFE simulation can be excluded.

5.3.2 Determination of optimal dimensions for sub-model

Although micro-scale RVE model is not applicable in holed specimens, the above-mentioned sensitivity studies with regard to mesh size and microstructure effects are still able to be applicable. The key issue at this scale is to determine an optimal dimension for the sub-model (see Fig. 6d) in the dual-scale FE simulation, which aims at least embedding the whole crack initiation zone at the holed root. As shown in Fig. 11a, from the view of macro-scale simulation, an obvious plastic deformation region for specimen H5 can be observed with an approximate length of 1.17 mm away from the holed root. In addition, the length of the corresponding crack zone is measured to be 1.19 mm based on SEM, seen in Fig. 11b.

From the view of micro-scale simulation, four different zones for CPFE model with the dimensions of 0.4 mm × 0.4 mm (V1), 0.8 mm × 0.8 mm (V2), 1.2 mm × 1.2 mm (V3) and 1.6 mm ×1.6 mm (V4) are selected, as shown in Fig. 12a. The crystallographic orientations and grain morphologies at holed root are the same for the four simulation zones. The maximum value of accumulated energy dissipation is used to be the evaluation criterion for selecting an optimal simulation zone as this value is essential for the crack initiation life prediction [59, 60]. After ten fatigue cycles with $\Delta\varepsilon_t$=0.4%, the hotspots of maximum accumulated energy dissipation is located in same grain except for the minimal finite element model (V1), as marked by red circles in Fig. 12b. In addition, the maximum values in the two neighboring grains are

extracted from these four cases (see in Fig. 12c), showing that the value is rarely influenced by the dimension of the sub-models of V3 and V4, with no more than 1% difference. Combined with the macro-scale simulation and SEM observation (see in Fig. 11), the dimensions of 1.2 mm × 1.2 mm were determined for the CPFE simulation.

5.4 Experimental creep-fatigue crack initiation life

In our previous studies [70, 71], the crack initiation life based on the metallographic observations referred to the cycle when the crack was firstly detected from the replica while it was not observed at last replica. Deng et al. [70] found that the fatigue crack initiation period occupied more than 90% of the total fatigue life for nickel-based GH4169 at 650 ℃. Wang et al. [71] investigated the interrupted creep-fatigue behavior based on the replica method and found that the small cracks initiate suddenly near micro-notch region and propagates quickly, leading to eventual material failure. In the above-mentioned studies, the pre-exiting defect or micro-crack in the tested specimens was used to determine the crack initiation sites and monitor the crack propagation behavior. However, for the holed specimen used in this work, the crack initiation sites were difficultly captured by using the current measurement techniques as the holed root lies inside the specimen. Therefore, an empirical approach was used to determine the crack initiation life. It indicated the most likely nucleation site to be located where the maximum load has dropped below 5% for nickel-based superalloys [60, 72], which was shown to be consistent with the previous experimental observation [70, 71].

The crack initiation life distributions of the uniaxial and holed specimens under both fatigue and creep-fatigue loading conditions for Inconel 718 are presented in Fig. 13a. As compared to uniaxial specimens, a more severe life reduction of holed specimens takes place with increasing hold times, especially for the specimen H10 with t_h=1800 s. For example, the creep-fatigue endurance for H10 reduces to about one-fourteenth of that without hold time. In order to investigate the hold time sensitivity, the life reduction factor, R_N, which is defined as the ratio of creep-fatigue crack initiation life against the fatigue one, is used to characterize the effect of hold time on creep-fatigue resistance of Inconel 718. The calculated results of R_N are shown in Fig. 13b. The results suggest that the value of F_r generally decreases with increasing the hold time for both uniaxial and holed specimens. In addition, the values of F_r are found to be in the range between 0.07 and 0.47 for holed specimen and those for uniaxial specimen are in the range between 0.27 and 0.56 when the hold time changes from 300 to 1800 s, indicating that creep-fatigue endurance of holed specimen is more sensitive to hold time than that of uniaxial specimen. It is noted that the stress concentration effect on creep-fatigue crack initiation life is related to shape, loading condition, material ductility and etc. As a brittle material Inconel 718, the hold time sensitivity to life reduction can be rationalized as that the stress re-distribution at stress concentration position (i.e. holed root) is relatively slow and the local accumulated plastic strain exceeds the limit required for fracture before attaining the stationary state [73].

5.5 Fractographic analysis

Fractographic analysis can be used to identify the creep-fatigue crack initiation mechanism under different hold times, where specimens H5 and H8 were regarded as typical loading conditions for comparison, as shown in Fig. 14. For the specimen H5, fatigue crack initiated at the specimen surface near to the holed root (Fig. 14a). Intensive fatigue striations were clearly observed at the crack propagation region, as shown in Figs. 14b and 14c. The arrangement of fatigue striations represented the crack propagation path, confirming crack propagated from the surface to the interior region [74]. For the specimen H8, crack initiation site was difficult to be distinguished at the holed root. Instead of fatigue striations, obvious intergranular facets and secondary cracks can be found in the vicinity of holed root (Fig. 14e), where long hold time played an important role in it.

6 Discussions

6.1 Stress-strain behaviors at holed root

The creep-fatigue behavior at holed root was analyzed, focusing on the plastic deformation and equivalent stress distributions. The simulated results for the representative specimen H8 are shown in Fig. 15, which illustrates qualitative and quantitative comparisons between the plastic strain, $\bar{\varepsilon}_p = \int_0^t \left(\frac{2}{3} \dot{\varepsilon}_p : \dot{\varepsilon}_p \right)^{1/2} dt$, in NU model and plastic slip, $p = \int_0^t \left(\frac{2}{3} \boldsymbol{L}_p : \boldsymbol{L}_p \right)^{1/2} dt$, in CP model at 1st, 4th and 8th cycles. A common tendency for accumulated $\bar{\varepsilon}_p$ and p was shown the contour maps (Figs. 15a-f) that both accumulated plastic deformations increased with increasing the

number of cycles. In addition, the obvious decreasing trends for the accumulated p and $\bar{\varepsilon}_p$ along the path a-a' (Figs.15a and 15d) can be observed from Figs. 15g-i. However, the distributions of p in contour maps were more fluctuant than those of $\bar{\varepsilon}_p$ due to taking grain morphology and grain orientation into account in CP model. Moreover, the peak values of p were obviously higher than those of $\bar{\varepsilon}_p$, see Figs. 15g-i. Following the above methodology, the qualitative and quantitative comparison between NU and CP models in terms of equivalent stress at the 8th cycle is shown in Fig. 16. The stress concentration effect is induced at holed root, so that the equivalent stress obtained from NU and CP models continuously decreased along the path a-a' (Figs. 16a and 16e). The values of relaxed stress extracted from NU model were about 36MPa, which coincided with the average relaxed stress extracted from CP model, see Figs. 16d and 16h. Different from the uniform stress field in NU model, the equivalent stress distributions in CP model were strongly influenced by the combined effects of grain orientation and geometric discontinuity, reflecting in the meandering stress distribution along the path a-a', as seen in Fig. 16h.

6.2 Creep and fatigue damage evolutions

The creep and fatigue damage evolutions in both macro- and micro-scale frameworks were discussed for the holed specimens. From the perspective of macro-scale, the creep and fatigue damage evolutions for specimen H8 along with the path from holed root to interior region (path b-b') are presented in Fig. 17a, where the maximum creep and fatigue damages occur at the surface near to the holed root at 100th cycle. Figure 17b presents the almost linear relations between accumulated

fatigue/creep damage ($D_{x,macro}=\sum_{j=1}^{N} d_{x,macro}^{(j)}$, $x=f$ and c) and the number of cycles for specimens H6 to H8, where the accumulated damages were extracted from the holed root pointed by the arrows in Fig. 17a. A general tendency in Fig. 17b visually shows that the fatigue damage is almost independent of hold time effect, while creep damage significantly increases with increasing hold times. From the perspective of micro-scale, Figure 18a gives the evolutional contour of energy dissipation with the number of cycles for the typical specimen H8, which owns potential capabilities in reflecting damage evolution process as well as identifying crack initiation sites [13, 33, 75]. The maximum accumulated energy dissipation was located position with a certain distance of several grain lengths from the holed root, which was defined as the hotspot in Fig. 18a. Local misorientation is quantified as Kernel Averaged Misorientation (KAM), regarding as a representative EBSD-based parameter to reveal the lattice curvature and localized inelastic deformation [76, 77]. The simulated location of maximum accumulated energy dissipation was in accord with that reflected in experimental KAM distribution map, where the highest KAM values mainly concentrated on some sub-surface grains, as indicated in Fig. 18b. Furthermore, Figure 18c exhibits that the magnitudes of accumulated energy dissipation at the hotspot linearly grown with increasing the number of cycles. As a result, the linearly increasing accumulated damages were consistent in macro- and micro-scale models. Regarding macro-scale damage evolution law up to 100 cycles (Fig. 17b) as the benchmark, it may provide an assistant support and precognition for the micro-scale damage calculation at higher cycles, which makes up for the deficiency of CPFE

simulation in calculation ability.

6.3 Creep-fatigue life prediction

In creep-fatigue loading conditions, the material deteriorates owing to simultaneous accumulations of time-dependent creep damage and cycle-dependent fatigue damage. With the aid of LDS rule, it is assumed that the final creep-fatigue life can be predicted when the summation of accumulated creep damage ($\sum_{j=1}^{N} d_c^{(j)}$) and accumulated fatigue damage ($\sum_{j=1}^{N} d_f^{(j)}$) equals to 1 at the most dangerous integration point near to holed root. Although the damage calculations of $d_c^{(j)}$ and $d_f^{(j)}$ come from different equations (Eqs. (9) and (11) for macro-scale damage models, Eqs. (23) and (24) for micro-scale damage models), both damage models share the same LDS rule to determine the final creep-fatigue life. In order to calculate the creep-fatigue crack initiation life, it is necessary to specify the two values of $W_{f,\mathrm{crit}}$ and $W_{c,\mathrm{crit}}$ in the prediction approach. During this process, an important issue must be mentioned that a linear relationship between FIPs (and CIPs) and the number of cycles has been confirmed in Fig. 18. Therefore, the predicted creep-fatigue crack initiation life can be written as

$$N_i = \frac{1}{W_{f,\mathrm{cyc}} \big/ W_{f,\mathrm{crit}} + W_{c,\mathrm{cyc}} \big/ W_{c,\mathrm{crit}}} \tag{26}$$

The life prediction results based on NU and CP models, where almost all the data points lie within ± 2 scatter band, as exhibited in Fig. 19. Results using the CP model show similar results to the NU model on life prediction. Therefore, the UN model is shown to be the best strategy to predict crack initiation life when the computational cost is not considered. Under the premise of promising prediction precisions, more

elaboration comparisons in prediction capabilities between the macro-scale damage models and micro-scale damage models are less meaningful. More advantages are manifested in the potential scientific and engineering meanings for the proposed dual-scale modelling approach in this work. From the scientific aspect, the dual-scale modelling approach provides an efficient methodology to take some microstructure factors (such as gradient microstructures, micro-defects, etc.) into account, which is difficult to be realized in the mature macro-scale framework. For the engineering aspect, several critical positions for the large components can be extracted by the "weakness identification technique" based on the macro-scale FE models. Aiming at these positions, full understanding of microscopic failure mechanisms based on micro-scale damage models can give some suggestions for unexpected failure prevention and life extension of the components.

7 Conclusions

A dual-scale modelling approach was developed to predict creep-fatigue life of holed specimens made by nickel-based Inconel 718 superalloy. The numerical framework integrating a non-unified model, crystal plasticity model and their corresponding damage-to-initiation models. Strain-controlled creep-fatigue tests for the specimens conducted at 650 ℃ were used to validate the performance of the dual-scale modelling approach. By applying post-test characterizations, the creep-fatigue crack iniation mechanisms under different loading conditions have been revealed. The main conclusions are summarized as follows:

(1) The predicted creep-fatigue crack initiation locations based on the dual-scale

modelling approach are in consistency with the microstructure observations using electron backscatter diffraction techniques.

(2) The linearly increasing accumulated damages are consistent in macro- and micro-scale models. Regarding macro-scale damage evolution law as the benchmark, it may provide an assistant support and precognition for the micro-scale damage calculation at higher cycles.

(3) The predicted creep-fatigue crack intiation life based on dual-scale modelling approach is in line with the experimental ones. Almost of the data points lie within ± 2 scatter band. Compared with the traditional numerical simulations, a significant improvement has been achived by applying the dual-scale modelling approach in the potential scientific and engineering applications.

Acknowledgements

This work was supported financially by the National Key Research and Development Program of China (2018YFC1902404), the National Natural Science Foundation of China (Nos. 52005185 and 51725503), China Postdoctoral Science Foundation (2020M681200) and 111 Project. Wang RZ and Miura H also gratefully acknowledge the support of the Postdoctoral Fellowships for Research in Japan (FY2020 P20350) by the Japan Society for the Promotion of Science (JSPS).

References

[1] R.P. Skelton, The energy density exhaustion method for assessing the creep-fatigue lives of specimens and components, Materials at High Temperatures, 30 (2014) 183-201.

[2] R.-Z. Wang, S.-J. Guo, H. Chen, J.-F. Wen, X.-C. Zhang, S.-T. Tu, Multi-axial creep-fatigue life prediction considering history-dependent damage evolution: A new numerical procedure and experimental validation, J. Mech. Phys. Solids, 131 (2019) 313-336.

[3] S.-P. Zhu, H.-Z. Huang, L.-P. He, Y. Liu, Z. Wang, A generalized energy-based fatigue–creep damage parameter for life prediction of turbine disk alloys, Engineering Fracture Mechanics, 90 (2012) 89-100.

[4] J. Juoksukangas, A. Lehtovaara, A. Mäntylä, Experimental and numerical investigation of fretting fatigue behavior in bolted joints, Tribology International, 103 (2016) 440-448.

[5] J. Wang, Y. Gao, Numerical and experimental investigations on fretting fatigue properties of GH4169 superalloy at the elevated temperature, International Journal of Fatigue, 149 (2021) 106274.

[6] J. Huo, D. Sun, H. Wu, W. Wang, l. Xue, Multi-axis low-cycle creep/fatigue life prediction of high-pressure turbine blades based on a new critical plane damage parameter, Engineering Failure Analysis, 106 (2019) 104159.

[7] M. Benedetti, F. Berto, L. Le Bone, C. Santus, A novel Strain-Energy-Density based fatigue criterion accounting for mean stress and plasticity effects on the medium-to-high-cycle uniaxial fatigue strength of plain and notched components, International Journal of Fatigue, 133 (2020) 105397.

[8] Y. Xu, W. Wan, F.P.E. Dunne, Microstructural fracture mechanics: Stored energy density at fatigue cracks, J. Mech. Phys. Solids, 146 (2021) 104209.

[9] J. Aktaa, R. Schmitt, High temperature deformation and damage behavior of RAFM steels under low cycle fatigue loading: Experiments and modeling, Fusion Engineering and Design, 81 (2006) 2221-2231.

[10] G. Cheng, A. Plumtree, A fatigue damage accumulation model based on continuum damage mechanics and ductility exhaustion, International Journal of Fatigue, 20 (1998) 495-501.

[11] T.D. Schwab, C.R. Johnston, T.R. Oxland, G.M. Thornton, Continuum damage mechanics (CDM) modelling demonstrates that ligament fatigue damage accumulates by different mechanisms than creep damage, Journal of Biomechanics, 40 (2007) 3279-3284.

[12] T.-W. Kim, D.-H. Kang, J.-T. Yeom, N.-K. Park, Continuum damage mechanics-based creep–fatigue-interacted life prediction of nickel-based superalloy at high temperature, Scripta Materialia, 57 (2007) 1149-1152.

[13] V.V.C. Wan, D.W. MacLachlan, F.P.E. Dunne, A stored energy criterion for fatigue crack nucleation in polycrystals, International Journal of Fatigue, 68 (2014) 90-102.

[14] R.P. Skelton, D. Gandy, Creep – fatigue damage accumulation and interaction diagram based on metallographic interpretation of mechanisms, Materials at High Temperatures, 25 (2014) 27-54.

[15] R. Wang, D. Li, D. Hu, F. Meng, H. Liu, Q. Ma, A combined critical distance and highly-stressed-volume model to evaluate the statistical size effect of the stress concentrator on low cycle fatigue of TA19 plate, International Journal of Fatigue, 95 (2017) 8-17.

[16] D. Liao, S.-P. Zhu, J.A.F.O. Correia, A.M.P. De Jesus, R. Calçada, Computational framework for multiaxial fatigue life prediction of compressor discs considering notch effects, Engineering Fracture Mechanics, 202 (2018) 423-435.

[17] C. Braccesi, G. Morettini, F. Cianetti, M. Palmieri, Development of a new simple energy method for life prediction in multiaxial fatigue, International Journal of Fatigue, 112 (2018) 1-8.

[18] E.S. Feng, X.G. Wang, C. Jiang, A new multiaxial fatigue model for life prediction based on energy dissipation evaluation, International Journal of Fatigue, 122 (2019) 1-8.

[19] E.L. Robinson, Effect of temperature variation on the long time strength of steels,

Trans. ASME, 74 (1952) 777-780.

[20] R.H. Priest, E.G. Ellison, A combined deformation map-ductility exhaustion approach to creep-fatigue analysis, Materials Science and Engineering, 49 (1981) 7-17.

[21] N.-K. Cho, R.-Z. Wang, Z. Ma, H. Chen, F.-Z. Xuan, Creep-fatigue endurance of a superheater tube plate under non-isothermal loading and multi-dwell condition, International Journal of Mechanical Sciences, 161-162 (2019) 105048.

[22] L. Xu, L. Zhao, Z. Gao, Y. Han, A novel creep–fatigue interaction damage model with the stress effect to simulate the creep–fatigue crack growth behavior, International Journal of Mechanical Sciences, 130 (2017) 143-153.

[23] S.V. Harren, H.E. Dève, R.J. Asaro, Shear band formation in plane strain compression, Acta Metall., 36 (1988) 2435-2480.

[24] A. Manonukul, F.P.E. Dunne, High- and Low-Cycle Fatigue Crack Initiation Using Polycrystal Plasticity, Mathematical, Physical and Engineering Sciences, 460 (2004) 1881-1903.

[25] R. Skelton, C. Rees, G.A. Webster, Energy damage summation methods for crack initiation and growth during block loading in high-temperature low-cycle fatigue, Fatigue & Fracture of Engineering Materials & Structures, 19 (1996) 287-297.

[26] N.G. Prastiti, Y. Xu, D.S. Balint, F.P.E. Dunne, Discrete dislocation, crystal plasticity and experimental studies of fatigue crack nucleation in single-crystal nickel, International Journal of Plasticity, 126 (2020) 102615.

[27] C.A. Sweeney, B. O'Brien, F.P.E. Dunne, P.E. McHugh, S.B. Leen, Strain-gradient modelling of grain size effects on fatigue of CoCr alloy, Acta Materialia, 78 (2014) 341-353.

[28] G.-J. Yuan, X.-C. Zhang, B. Chen, S.-T. Tu, C.-C. Zhang, Low-cycle fatigue life prediction of a polycrystalline nickel-base superalloy using crystal plasticity modelling approach, Journal of Materials Science & Technology, 38 (2020) 28-38.

[29] O.J. McCarthy, J.P. McGarry, S.B. Leen, The effect of grain orientation on fretting fatigue plasticity and life prediction, Tribology International, 76 (2014) 100-115.

[30] J. Wang, T. Chen, C. Zhou, Crystal plasticity modeling of fretting fatigue behavior of an aluminum alloy, Tribology International, 156 (2021) 106841.

[31] P.J. Ashton, A.M. Harte, S.B. Leen, A strain-gradient, crystal plasticity model for microstructure-sensitive fretting crack initiation in ferritic-pearlitic steel for flexible marine risers, International Journal of Fatigue, 111 (2018) 81-92.

[32] V.V.C. Wan, M.A. Cuddihy, J. Jiang, D.W. MacLachlan, F.P.E. Dunne, An HR-EBSD and computational crystal plasticity investigation of microstructural stress distributions and fatigue hotspots in polycrystalline copper, Acta Materialia, 115 (2016) 45-57.

[33] B. Chen, J. Jiang, F.P.E. Dunne, Is stored energy density the primary meso-scale mechanistic driver for fatigue crack nucleation?, International Journal of Plasticity, 101 (2018) 213-229.

[34] Y. Su, Q.-N. Han, W. Qiu, Z. He, Y.-B. Shang, H.-J. Shi, L.-S. Niu, High temperature in-situ SEM observation and crystal plasticity simulation on fretting fatigue of Ni-based single crystal superalloys, International Journal of Plasticity, 127 (2020) 102645.

[35] K.-S. Li, R.-Z. Wang, G.-J. Yuan, S.-P. Zhu, X.-C. Zhang, S.-T. Tu, H. Miura, A crystal plasticity-based approach for creep-fatigue life prediction and damage evaluation in a nickel-based superalloy, International Journal of Fatigue, 143 (2021) 106031.

[36] S. Park, J. Jung, W. Cho, B.-S. Jeong, H. Na, S.-I. Kim, M.-G. Lee, H.N. Han, Predictive dual-scale finite element simulation for hole expansion failure of ferrite-bainite steel, International Journal of Plasticity, 136 (2021) 102900.

[37] L. Li, L. Shen, G. Proust, Fatigue crack initiation life prediction for aluminium alloy 7075 using crystal plasticity finite element simulations, Mechanics of Materials, 81 (2015) 84-93.

[38] E.D. Meade, F. Sun, P. Tiernan, N.P. O'Dowd, Experimental study and multiscale modelling of the high temperature deformation of tempered martensite under multiaxial loading, Materials Science and Engineering: A, 737 (2018) 383-392.

[39] G. Hu, S. Huang, D. Lu, X. Zhong, Z. Li, W. Brocks, K. Zhang, Subsequent

yielding of polycrystalline aluminum after cyclic tension–compression analyzed by experiments and simulations, International Journal of Solids and Structures, 56-57 (2015) 142-153.

[40] F. Briffod, T. Shiraiwa, M. Enoki, Microstructure modeling and crystal plasticity simulations for the evaluation of fatigue crack initiation in α-iron specimen including an elliptic defect, Materials Science and Engineering: A, 695 (2017) 165-177.

[41] M. Dabiri, M. Lindroos, T. Andersson, S. Afkhami, A. Laukkanen, T. Björk, Utilizing the theory of critical distances in conjunction with crystal plasticity for low-cycle notch fatigue analysis of S960 MC high-strength steel, International Journal of Fatigue, 117 (2018) 257-273.

[42] X. Shang, H. Zhang, Z. Cui, M.W. Fu, J. Shao, A multiscale investigation into the effect of grain size on void evolution and ductile fracture: Experiments and crystal plasticity modeling, International Journal of Plasticity, 125 (2020) 133-149.

[43] M. Kobayashi, M. Mukai, H. Takahashi, N. Ohno, T. Kawakami, T. Ishikawa, Implicit integration and consistent tangent modulus of a time-dependent non-unified constitutive model, International Journal for Numerical Methods in Engineering, 58 (2003) 1523-1543.

[44] L. Meng, W. Chen, Y. Yan, T. Kitamura, M. Feng, Modelling of creep and plasticity deformation considering creep damage and kinematic hardening, Engineering Fracture Mechanics, 218 (2019) 106582.

[45] L.-Y. Cheng, R.-Z. Wang, J. Wang, S.-P. Zhu, P.-C. Zhao, H. Miura, X.-C. Zhang, S.-T. Tu, Cycle-dependent creep-fatigue deformation and life predictions in a nickel-based superalloy at elevated temperature, International Journal of Mechanical Sciences, 206 (2021) 106628.

[46] R. Ahmed, P.R. Barrett, T. Hassan, Unified viscoplasticity modeling for isothermal low-cycle fatigue and fatigue-creep stress–strain responses of Haynes 230, International Journal of Solids and Structures, 88-89 (2016) 131-145.

[47] R.-Z. Wang, S.-P. Zhu, J. Wang, X.-C. Zhang, S.-T. Tu, C.-C. Zhang, High temperature fatigue and creep-fatigue behaviors in a Ni-based superalloy: Damage mechanisms and life assessment, International Journal of Fatigue, 118 (2019) 8-21.

[48] A. Banerjee, J.K. Sahu, N. Paulose, C.D. Fernando, R.N. Ghosh, Micromechanism of cyclic plastic deformation of alloy IN 718 at 600 °C, Fatigue & Fracture of Engineering Materials & Structures, 39 (2016) 877-885.

[49] R.-Z. Wang, X.-C. Zhang, S.-T. Tu, S.-P. Zhu, C.-C. Zhang, A modified strain energy density exhaustion model for creep–fatigue life prediction, International Journal of Fatigue, 90 (2016) 12-22.

[50] W.M. Payten, D.W. Dean, K.U. Snowden, A strain energy density method for the prediction of creep–fatigue damage in high temperature components, Materials Science and Engineering: A, 527 (2010) 1920-1925.

[51] Z. Li, D. Shi, S. Li, X. Yang, G. Miao, A systematical weight function modified critical distance method to estimate the creep-fatigue life of geometrically different structures, International Journal of Fatigue, 126 (2019) 6-19.

[52] F. Ellyin, K. Golos, Multiaxial Fatigue Damage Criterion, Journal of Engineering Materials and Technology, 110 (1988) 63-68.

[53] E.P. Busso, A continuum theory for dynamic recrystallization with microstructure-related length scales, International Journal of Plasticity, 14 (1998) 319-353.

[54] D.-F. Li, C.M. Davies, S.-Y. Zhang, C. Dickinson, N.P. O'Dowd, The effect of prior deformation on subsequent microplasticity and damage evolution in an austenitic stainless steel at elevated temperature, Acta Materialia, 61 (2013) 3575-3584.

[55] S. Keshavarz, S. Ghosh, Multi-scale crystal plasticity finite element model approach to modeling nickel-based superalloys, Acta Materialia, 61 (2013) 6549-6561.

[56] D.-F. Li, R.A. Barrett, P.E. O'Donoghue, N.P. O'Dowd, S.B. Leen, A multi-scale crystal plasticity model for cyclic plasticity and low-cycle fatigue in a precipitate-strengthened steel at elevated temperature, J. Mech. Phys. Solids, 101 (2017) 44-62.

[57] D.-F. Li, B.J. Golden, N.P. O'Dowd, Multiscale modelling of mechanical response in a martensitic steel: A micromechanical and length-scale-dependent

framework for precipitate hardening, Acta Materialia, 80 (2014) 445-456.

[58] K.-S. Zhang, J.W. Ju, Z. Li, Y.-L. Bai, W. Brocks, Micromechanics based fatigue life prediction of a polycrystalline metal applying crystal plasticity, Mechanics of Materials, 85 (2015) 16-37.

[59] A. Korsunsky, D. Dini, F. Dunne, M. Walsh, Comparative assessment of dissipated energy and other fatigue criteria☆, International Journal of Fatigue, 29 (2007) 1990-1995.

[60] A. Cruzado, S. Lucarini, J. Llorca, J. Segurado, Microstructure-based fatigue life model of metallic alloys with bilinear Coffin-Manson behavior, International Journal of Fatigue, 107 (2018) 40-48.

[61] X. Sun, K.S. Choi, W.N. Liu, M.A. Khaleel, Predicting failure modes and ductility of dual phase steels using plastic strain localization, International Journal of Plasticity, 25 (2009) 1888-1909.

[62] H. Liu, D. Hu, R. Wang, X. Wang, S. Jin, Y. Gu, Experimental and numerical investigations on the influence of cold expansion on low cycle fatigue life of bolt holes in aeroengine superalloy disk at elevated temperature, International Journal of Fatigue, 132 (2020) 105390.

[63] G. Kang, Q. Gao, X. Yang, A visco–plastic constitutive model incorporated with cyclic hardening for uniaxial/multiaxial ratcheting of SS304 stainless steel at room temperature, Mechanics of Materials, 34 (2002) 521-531.

[64] X. Wang, Y. Jiang, J. Gong, Y. Zhao, X. Huang, Characterization of Low Cycle Fatigue of Ferritic-Martensitic P92 Steel: Effect of Temperature, steel research international, 87 (2016) 761-771.

[65] R.-Z. Wang, X.-C. Zhang, J.-G. Gong, X.-M. Zhu, S.-T. Tu, C.-C. Zhang, Creep-fatigue life prediction and interaction diagram in nickel-based GH4169 superalloy at 650°C based on cycle-by-cycle concept, International Journal of Fatigue, 97 (2017) 114-123.

[66] E.P. Busso, F.T. Meissonnier, N.P. O'Dowd, Gradient-dependent deformation of two-phase single crystals, J. Mech. Phys. Solids, 48 (2000) 2333-2361.

[67] B. Lin, L.G. Zhao, J. Tong, H.J. Christ, Crystal plasticity modeling of cyclic deformation for a polycrystalline nickel-based superalloy at high temperature, Materials Science and Engineering: A, 527 (2010) 3581-3587.

[68] A. Cruzado, S. Lucarini, J. Llorca, J. Segurado, Crystal plasticity simulation of the effect of grain size on the fatigue behavior of polycrystalline Inconel 718, International Journal of Fatigue, 113 (2018) 236-245.

[69] R.-Z. Wang, C. Bo, X.-C. Zhang, S.-T. Tu, W. Ji, C.-C. Zhang, The effects of inhomogeneous microstructure and loading waveform on creep-fatigue behaviour in a forged and precipitation hardened nickel-based superalloy, International Journal of Fatigue, 97 (2017) 190-201.

[70] G.-J. Deng, S.-T. Tu, X.-C. Zhang, J. Wang, C.-C. Zhang, X.-Y. Qian, Y.-N. Wang, Small fatigue crack initiation and growth mechanisms of nickel-based superalloy GH4169 at 650°C in air, Engineering Fracture Mechanics, 153 (2016) 35-49.

[71] J. Wang, R.-Z. Wang, X.-C. Zhang, Y.-J. Ye, Y. Cui, H. Miura, S.-T. Tu, Multi-stage dwell fatigue crack growth behaviors in a nickel-based superalloy at elevated temperature, Engineering Fracture Mechanics, 253 (2021) 107859.

[72] A.B. Thakker, B.A. Cowles, Low strain, long life creep fatigue of AF2-1DA and INCO 718, in, 1983.

[73] J.-G. Gong, G. Cheng, F.-Z. Xuan, H. Chen, Notch Effect on Structural Strength of Components at Elevated Temperature Under Creep, Fatigue, and Creep-Fatigue Loading Conditions: Phenomenon and Mechanism, Journal of Pressure Vessel Technology, 141 (2019).

[74] J.C. Stinville, E. Martin, M. Karadge, S. Ismonov, M. Soare, T. Hanlon, S. Sundaram, M.P. Echlin, P.G. Callahan, W.C. Lenthe, V.M. Miller, J. Miao, A.E. Wessman, R. Finlay, A. Loghin, J. Marte, T.M. Pollock, Fatigue deformation in a polycrystalline nickel base superalloy at intermediate and high temperature: Competing failure modes, Acta Materialia, 152 (2018) 16-33.

[75] X. Lu, F.P.E. Dunne, Y. Xu, A crystal plasticity investigation of slip system interaction, GND density and stored energy in non-proportional fatigue in

Nickel-based superalloy, International Journal of Fatigue, 139 (2020) 105782.
[76] Y. Ogawa, D. Birenis, H. Matsunaga, O. Takakuwa, J. Yamabe, Ø. Prytz, A. Thøgersen, The role of intergranular fracture on hydrogen-assisted fatigue crack propagation in pure iron at a low stress intensity range, Materials Science and Engineering: A, 733 (2018) 316-328.
[77] S.-S. Rui, Y.-B. Shang, Y. Su, W. Qiu, L.-S. Niu, H.-J. Shi, S. Matsumoto, Y. Chuman, EBSD analysis of cyclic load effect on final misorientation distribution of post-mortem low alloy steel: A new method for fatigue crack tip driving force prediction, International Journal of Fatigue, 113 (2018) 264-276.

List of Figure captions

Figure 1 Technological process and parameters of standard heat treatment contained one-stage solid solution and two-stage aging treatments, and the microstructure of inverse pole figure after standard heat treatment obtained by EBSD technique for Inconel 718.

Figure 2 Testing operation system and temperature measurement system on MTS testing machine: (a) two ceramic rods of a high-temperature extensometer symmetrically attached to the gauge-length area of the holed specimen, (b) placement of the high-temperature furnace during heating, (c) internal structure of the high-temperature furnace, (d) two temperature controllers including upper element and lower element.

Figure 3 Overall flow chart of dual-scale modelling approach for predicting creep-fatigue crack initiation life of holed specimens, and the macro-scale framework as benchmark and micro-scale framework as objective.

Figure 4 Schematic diagram illustrating definition of strain energy density: (a) elastic and plastic strain energy density; (b) creep strain energy density.

Figure 5 Macro-scale modelling approach and corresponding boundary conditions: (a) RVE model for uniaxial specimens; (b) FE model in gauge-section for holed specimens.

Figure 6 Micro-scale modelling approach: (a) micro-scale RVE model for uniaxial specimens; Dual-scale modelling approach: (b) the whole holed specimen, (c)

macro-scale FE model for the holed specimen; (d) CPFE model applied in the holed root.

Figure 7 Flowcharts of the calibration procedures to determine model parameters: (a) NU model parameters; (b) CP model parameters.

Figure 8 Fitting the relation between the number of fatigue cycles to crack initiation and total strain energy density in macro-scale damage model.

Figure 9 Comparison between experimental data and simulated results based on both NU model and CP model for specimens U3, U6 and U10: (a-c) hysteresis loops at the first cycle; (d-f) stress relaxation at the first cycle; (g-i) the maximum error analysis between the experimental and simulation stress.

Figure 10 Sensitivity studies in CPFE simulation for Inconel 718: (a) Comparisons of tensile curves and accumulated energy dissipation using coarse, medium and fine mesh; (b) comparisons of tensile curves and accumulated energy dissipation using different microstructures of M1, M2 and M3.

Figure 11 Determination of the dimensions for the sub-model in dual-scale FE simulation: (a) the macro-scale FE simulation and fatigued specimen; (b) SEM micrograph of overall fracture appearance; (c) the dimensions for the sub-model.

Figure 12 Comparison of four different zones of the CPFE model with the selected lengths of 0.4 mm × 0.4 mm (V1), 0.8 mm × 0.8 mm (V2), 1.2 mm × 1.2 mm (V3) and 1.6 mm × 1.6 mm (V4): (a) four grain morphologies, (b) contour

maps of accumulated energy dissipation, (c) the nominalized path a-a′ in two grains of energy dissipation evolution profile.

Figure 13 (a) Experimental crack initiation life distributions with hold time, and (b) life reduction factor at different total strain ranges for the uniaxial and holed specimens subjected to fatigue and creep-fatigue loading conditions in Inconel 718 at 650 °C.

Figure 14 SEM micrographs of different failure modes for holed specimens under different loading conditions: (a)-(c) specimen H5 under fatigue loading condition with $\Delta\varepsilon_t$=0.4%; (d)-(f) specimen H8 under creep-fatigue loading condition with $\Delta\varepsilon_t$=0.4% and t_h=1800 s.

Figure 15 Accumulated plastic deformation at different cycles of specimen H8 under creep-fatigue loading condition with $\Delta\varepsilon_t$=0.4% and t_h=1800 s for Inconel 718: (a-c) contour maps of equivalent plastic strain based on NU model; (d-f) contour maps of plastic slip based on CP model; (g-f) comparisons between the plastic deformations in the two constitutive models.

Figure 16 Equivalent stress evolutions at hold-begin, hold-end and valley for specimen H8 under creep-fatigue with $\Delta\varepsilon_t$=0.4% and t_h=1800 s at 8th cycle: (a-d) simulated results based on NU model; (e-h) simulated results based on CP model.

Figure 17 Creep damage and fatigue damage evolutions from macro-scale FE model: (a) the distributions of creep damage and fatigue damage per cycle along the path b-b’ for specimen H8 under creep-fatigue loading condition with

$\Delta\varepsilon_t$=0.4% and t_h =1800s at 30th cycle; (b) relations between accumulated creep damage and fatigue damage and the number of cycles for the specimens with $\Delta\varepsilon_t$=0.4% and different hold times.

Figure 18 Damage evolutions from simulated results and experimental observation: (a) accumulated energy dissipation contour at 8th cycle and (b) KAM distribution map at holed root for specimen H8 under creep-fatigue loading condition with $\Delta\varepsilon_t$=0.4% and t_h =1800s; (c) the relation between accumulated energy dissipation and the number of cycles under different loading conditions.

Figure 19 Comparisons between experimental creep-fatigue crack initiation life and predicted results based on NU model and CP model for holed specimens under different loading conditions in Inconel 718.

List of Table captions

Table 1 Detailed parameters of the uniaxial round bar and central circular hole specimens in creep-fatigue tests for Inconel 718.

Table 2 Material parameters of NU model for Inconel 718 at 650 ℃.

Table 3 Material parameters in CP model for Inconel 718 at 650 ℃.

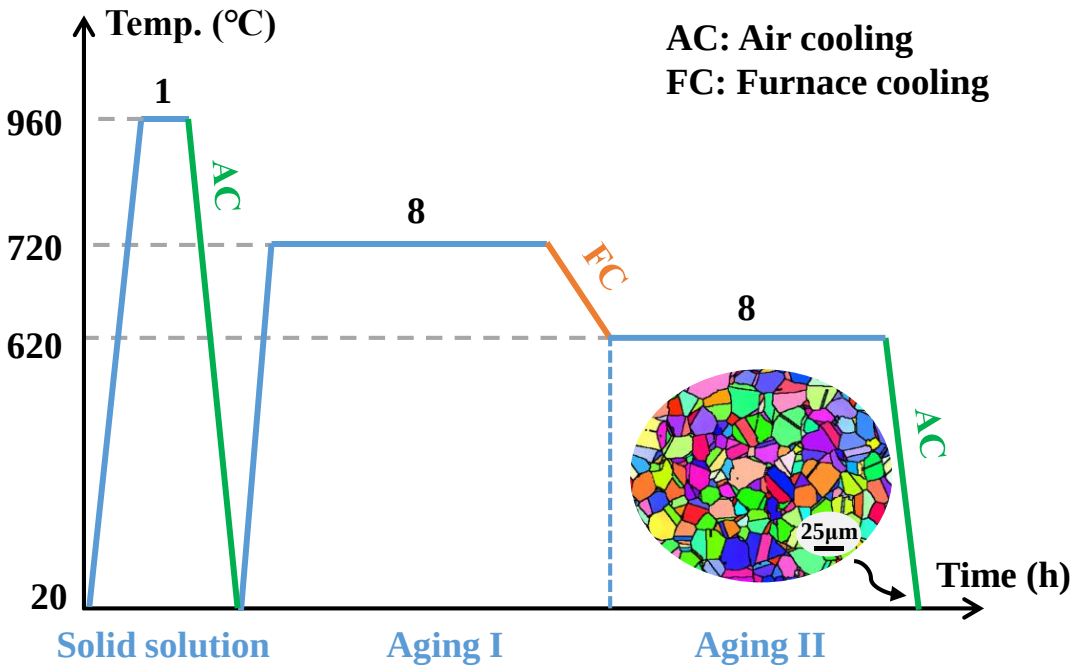

Figure 1 Technological process and parameters of standard heat treatment contained one-stage solid solution and two-stage aging treatments, and the microstructure of inverse pole figure after standard heat treatment obtained by EBSD technique for Inconel 718.

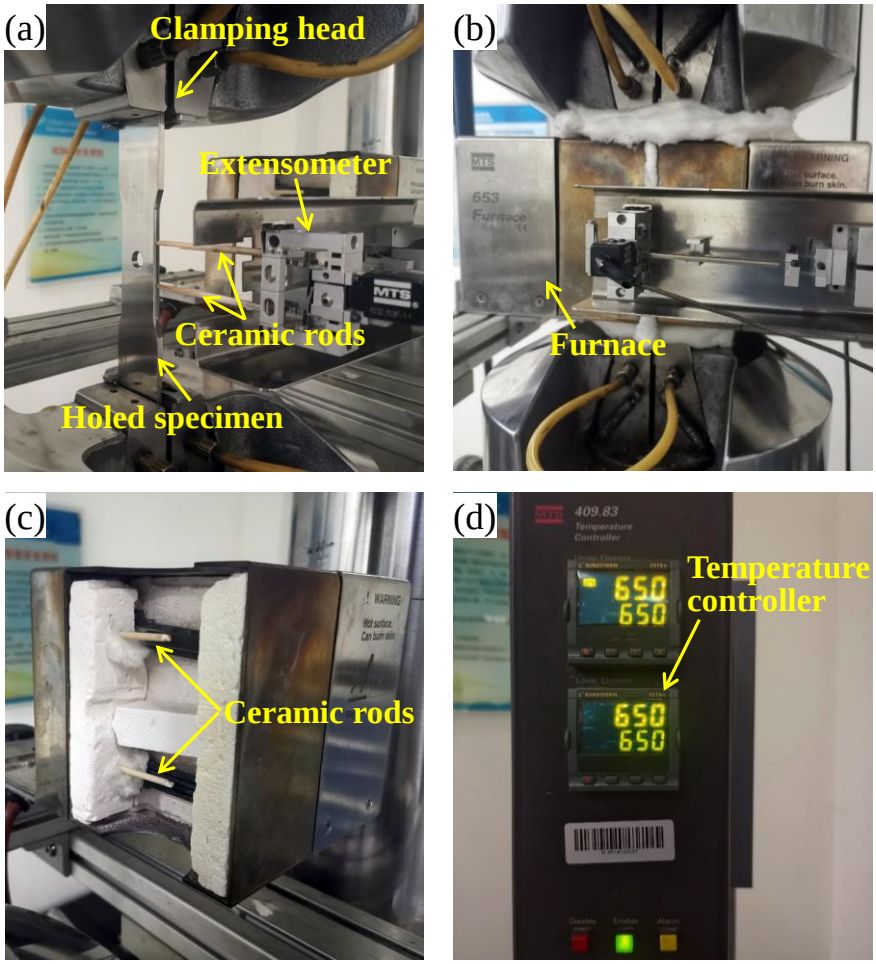

Figure 2 Testing operation system and temperature measurement system on MTS testing machine: (a) two ceramic rods of a high-temperature extensometer symmetrically attached to the gauge-length area of the holed specimen, (b) placement of the high-temperature furnace during heating, (c) internal structure of the high-temperature furnace, (d) two temperature controllers including upper element and lower element.

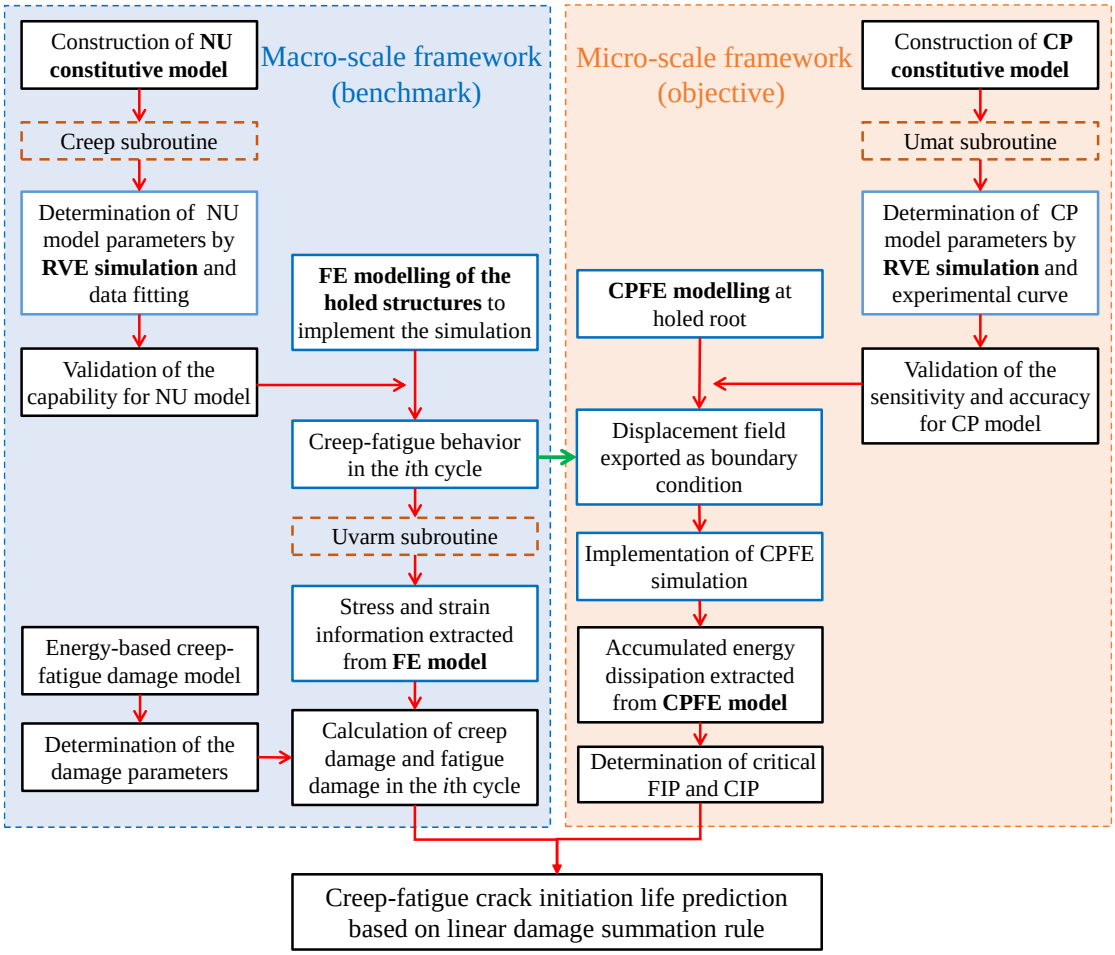

Figure 3 Overall flow chart of dual-scale modelling approach for predicting creep-fatigue crack initiation life of holed specimens, and the macro-scale framework as benchmark and micro-scale framework as objective.

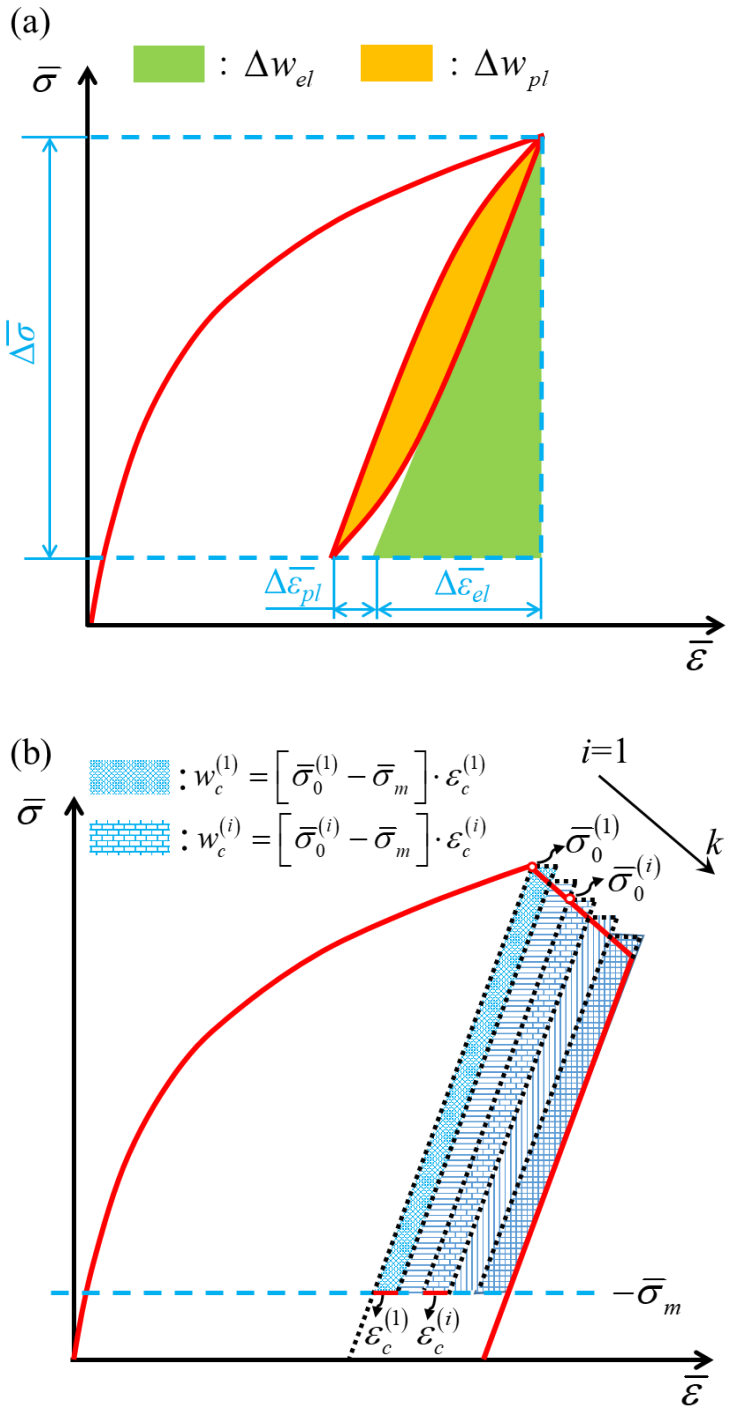

Figure 4 Schematic diagram illustrating definition of strain energy density: (a) elastic and plastic strain energy density; (b) creep strain energy density.

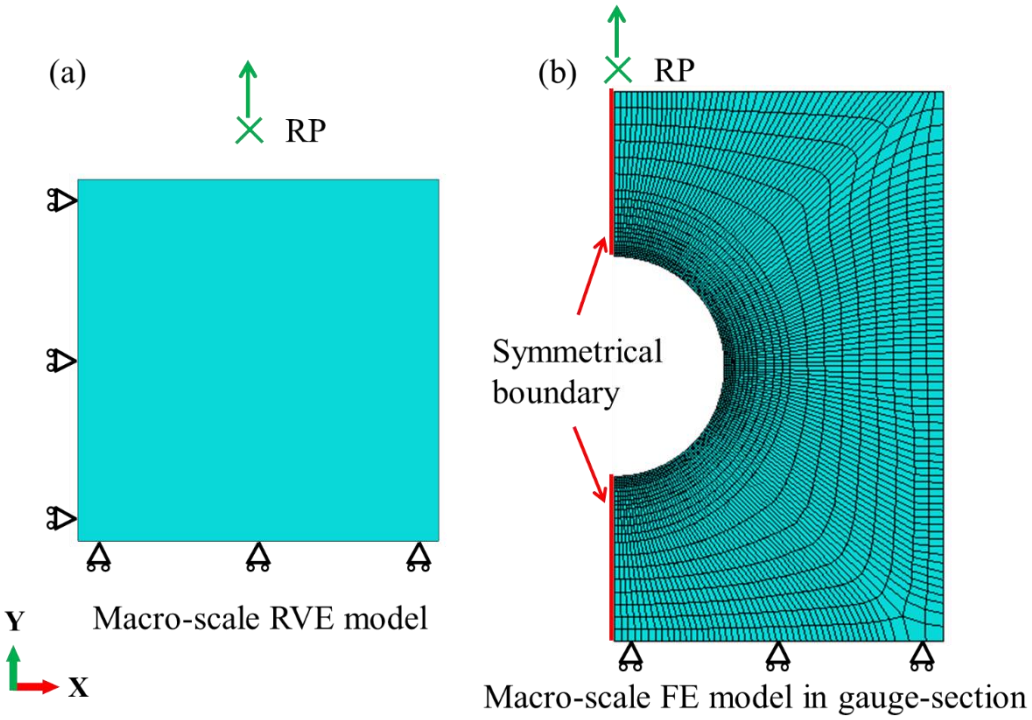

Figure 5 Macro-scale modelling approach and corresponding boundary conditions: (a) RVE model for uniaxial specimens; (b) FE model in gauge-section for holed specimens.

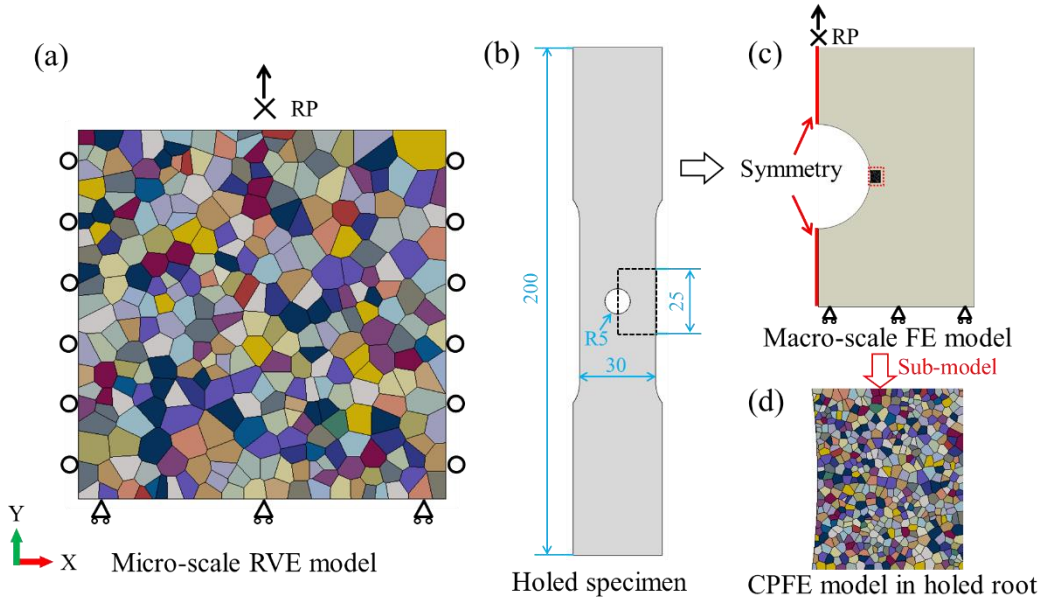

Figure 6 Micro-scale modelling approach: (a) micro-scale RVE model for uniaxial specimens; Dual-scale modelling approach: (b) the whole holed specimen, (c) macro-scale FE model for the holed specimen; (d) CPFE model applied in the holed root.

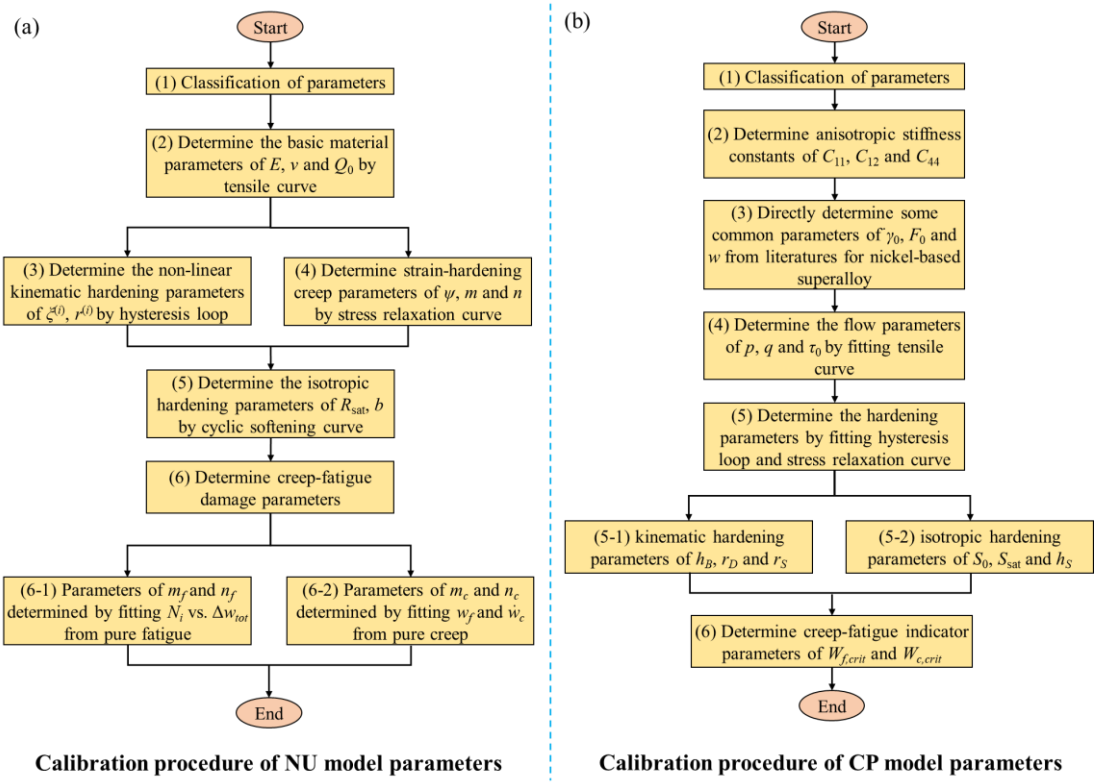

Figure 7 Flowcharts of the calibration procedures to determine model parameters: (a) NU model parameters; (b) CP model parameters.

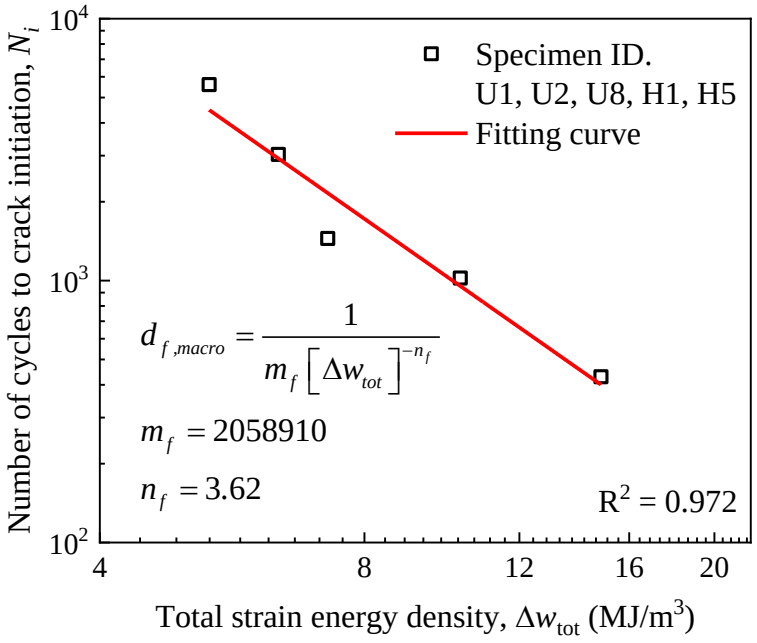

Figure 8 Fitting the relation between the number of fatigue cycles to crack initiation and total strain energy density in macro-scale damage model.

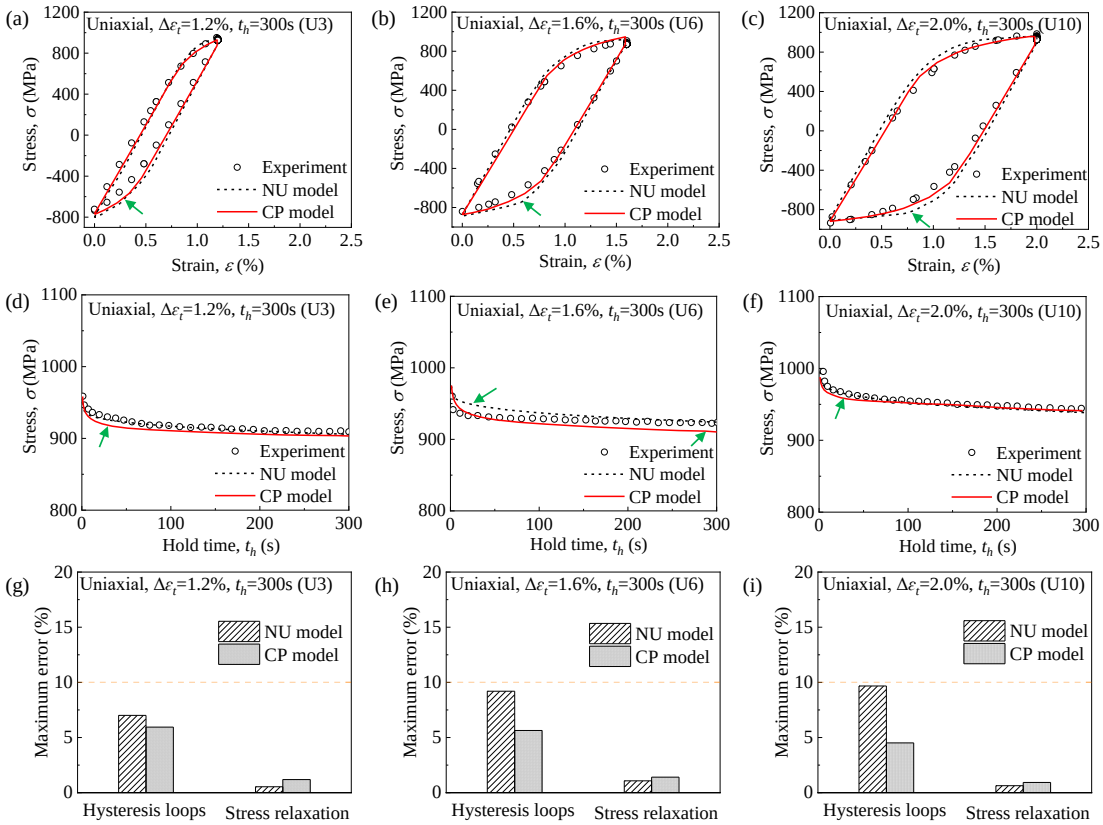

Figure 9 Comparison between experimental data and simulated results based on both NU model and CP model for specimens U3, U6 and U10: (a-c) hysteresis loops at the first cycle; (d-f) stress relaxation at the first cycle; (g-i) the maximum error analysis between the experimental and simulation stress.

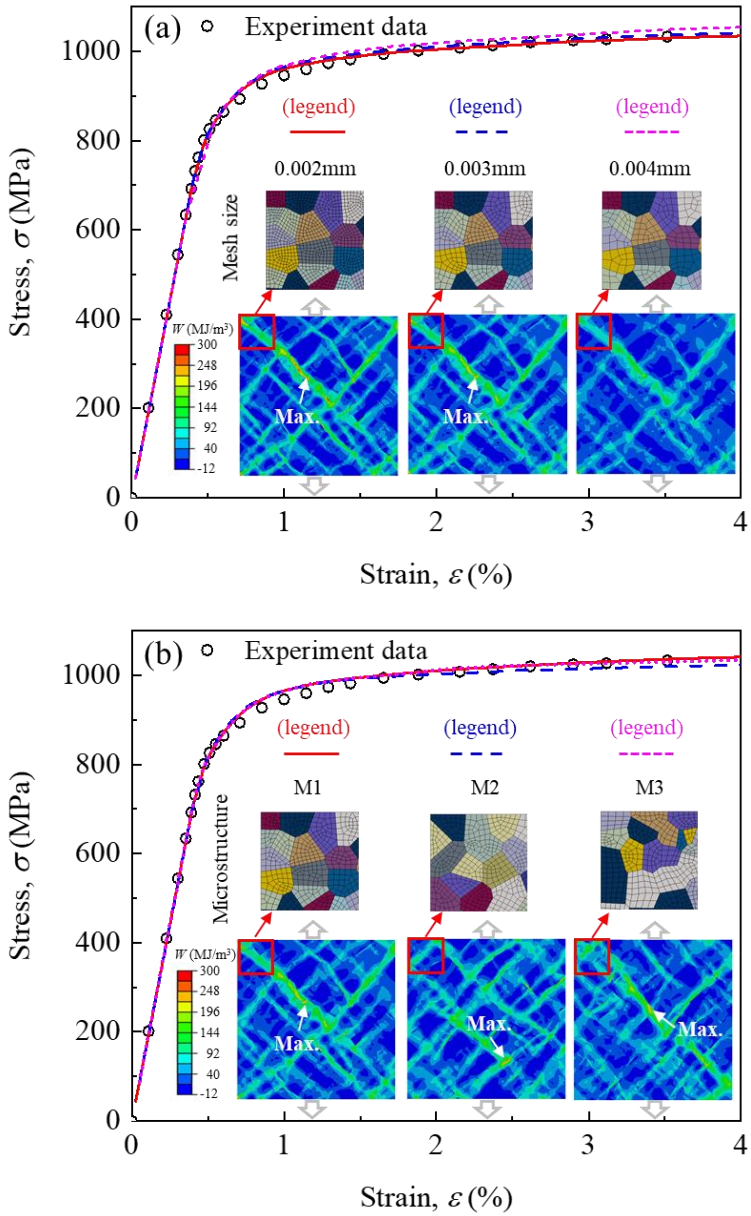

Figure 10 Sensitivity studies in CPFE simulation for Inconel 718: (a) Comparisons of tensile curves and accumulated energy dissipation using coarse, medium and fine mesh; (b) comparisons of tensile curves and accumulated energy dissipation using different microstructures of M1, M2 and M3.

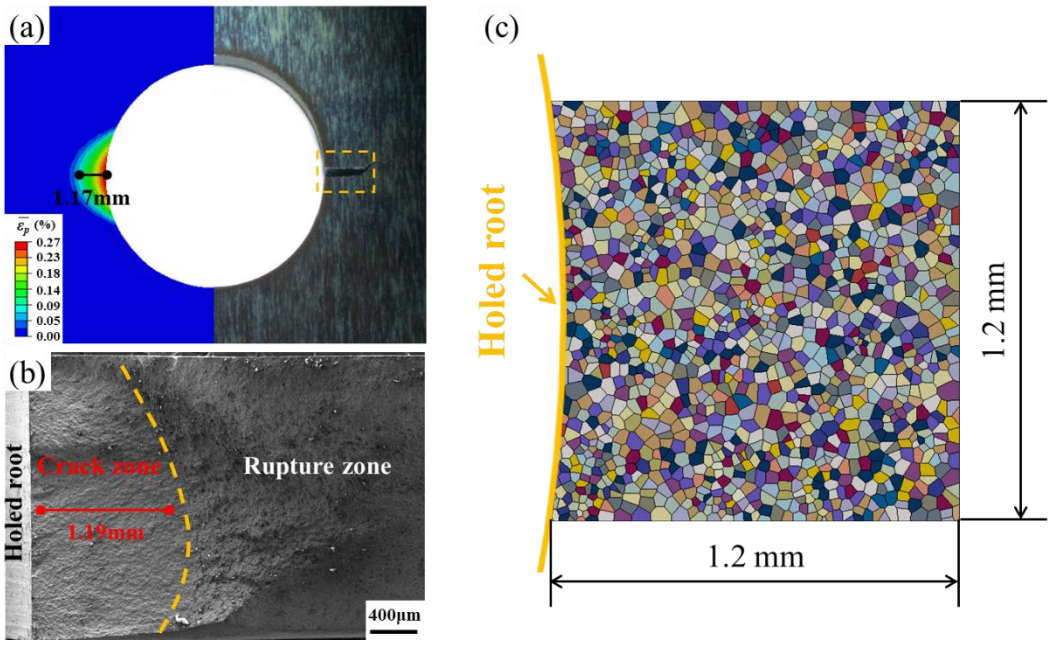

Figure 11 Determination of the dimensions for the sub-model in dual-scale FE simulation: (a) the macro-scale FE simulation and fatigued specimen; (b) SEM micrograph of overall fracture appearance; (c) the dimensions for the sub-model.

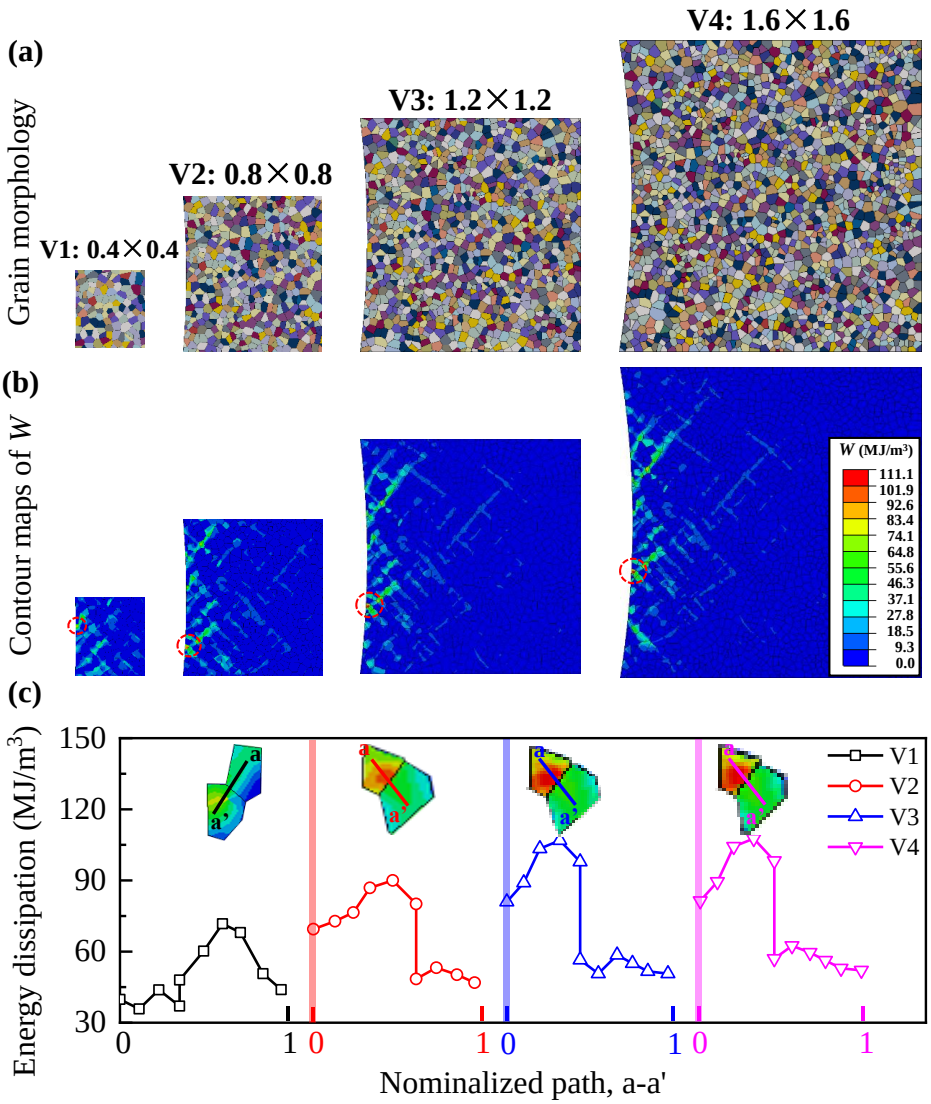

Figure 12 Comparison of four different zones of the CPFE model with the selected lengths of 0.4 mm × 0.4 mm (V1), 0.8 mm × 0.8 mm (V2), 1.2 mm × 1.2 mm (V3) and 1.6 mm × 1.6 mm (V4): (a) four grain morphologies, (b) contour maps of accumulated energy dissipation, (c) the nominalized path a-a′ in two grains of energy dissipation evolution profile.

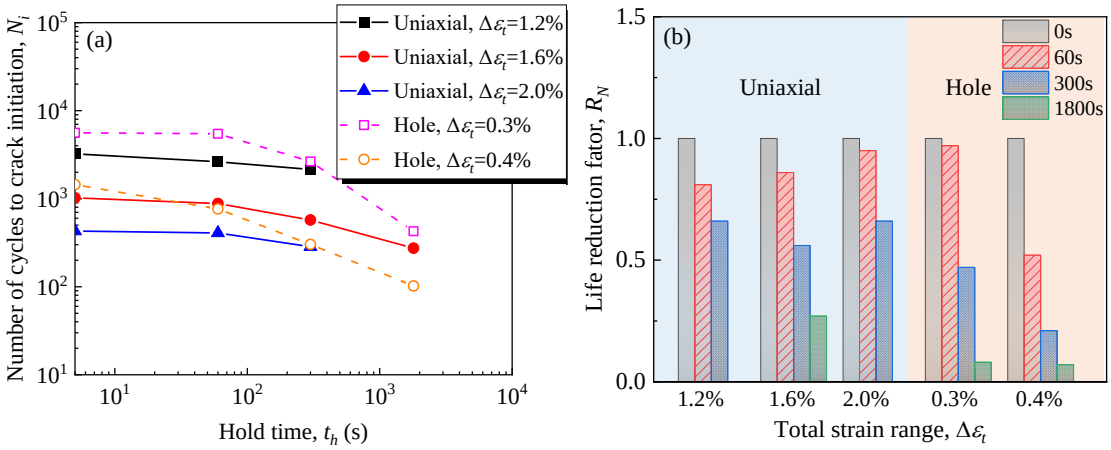

Figure 13 (a) Experimental crack initiation life distributions with hold time, and (b) life reduction factor at different total strain ranges for the uniaxial and holed specimens subjected to fatigue and creep-fatigue loading conditions in Inconel 718 at 650 °C.

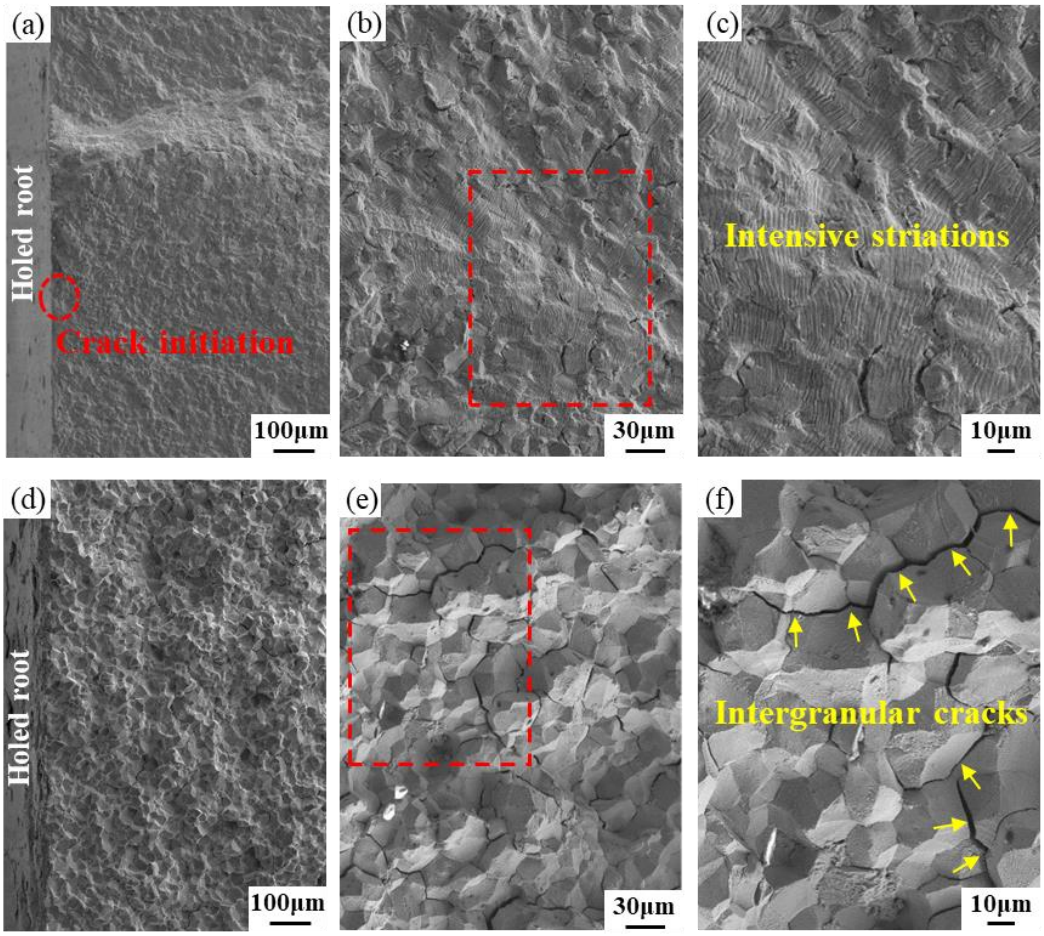

Figure 14 SEM micrographs of different failure modes for holed specimens under different loading conditions: (a)-(c) specimen H5 under fatigue loading condition with $\Delta\varepsilon_t$=0.4%; (d)-(f) specimen H8 under creep-fatigue loading condition with $\Delta\varepsilon_t$=0.4% and t_h=1800 s.

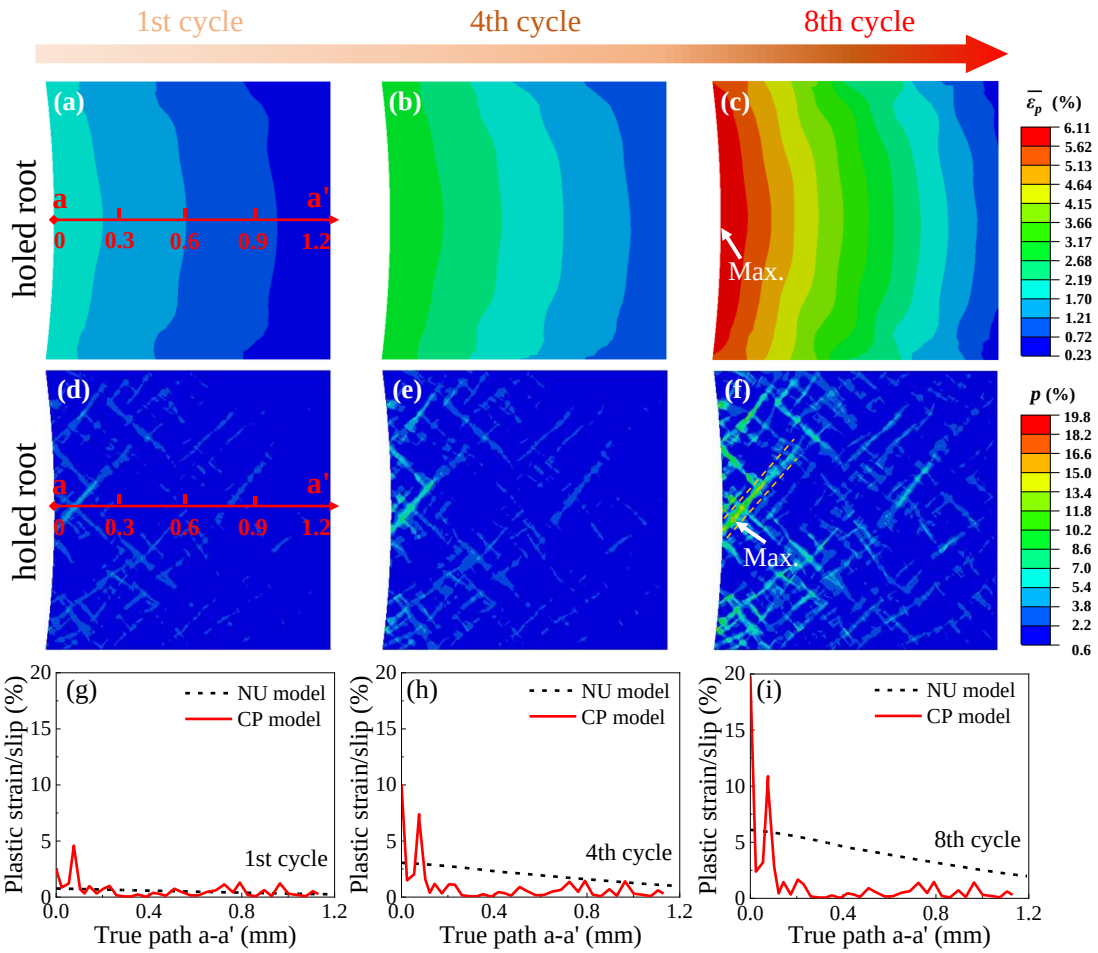

Figure 15 Accumulated plastic deformation at different cycles of specimen H8 under creep-fatigue loading condition with $\Delta\varepsilon_t$=0.4% and t_h=1800 s for Inconel 718: (a-c) contour maps of equivalent plastic strain based on NU model; (d-f) contour maps of plastic slip based on CP model; (g-f) comparisons between the plastic deformations in the two constitutive models.

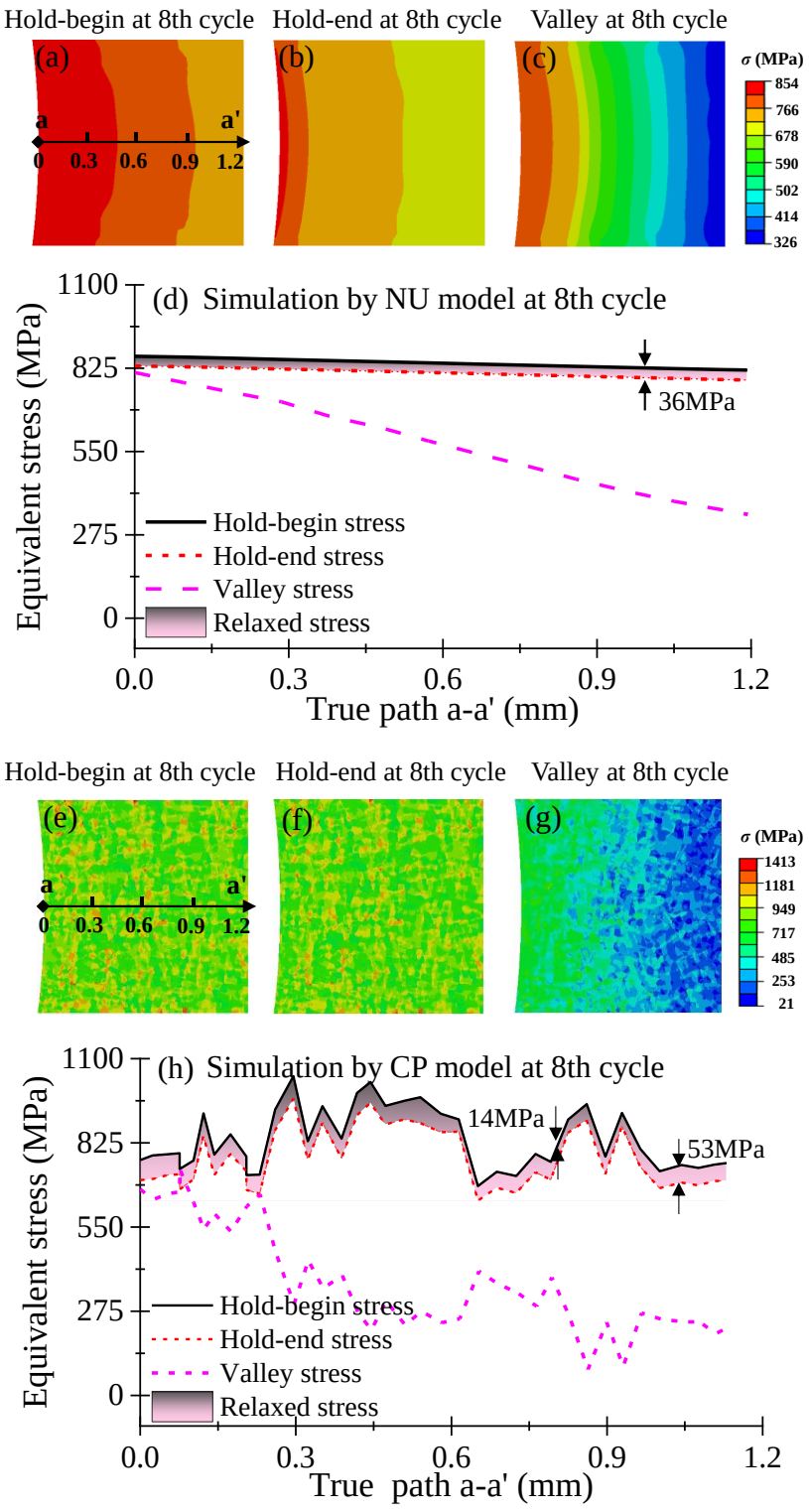

Figure 16 Equivalent stress evolutions at hold-begin, hold-end and valley for specimen H8 under creep-fatigue with $\Delta\varepsilon_t$=0.4% and t_h=1800 s at 8th cycle: (a-d) simulated results based on NU model; (e-h) simulated results based on CP model.

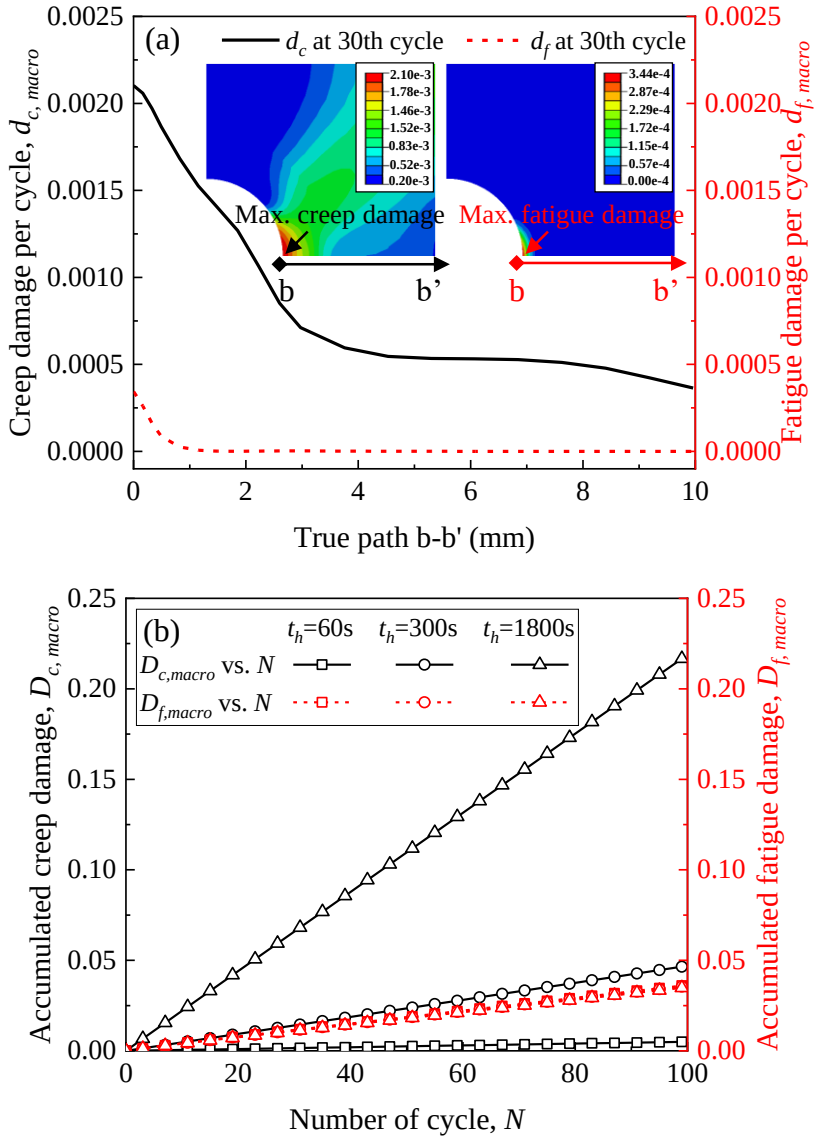

Figure 17 Creep damage and fatigue damage evolutions from macro-scale FE model: (a) the distributions of creep damage and fatigue damage per cycle along the path b-b' for specimen H8 under creep-fatigue loading condition with $\Delta\varepsilon_t$=0.4% and t_h =1800s at 30th cycle; (b) relations between accumulated creep damage and fatigue damage and the number of cycles for the specimens with $\Delta\varepsilon_t$=0.4% and different hold times.

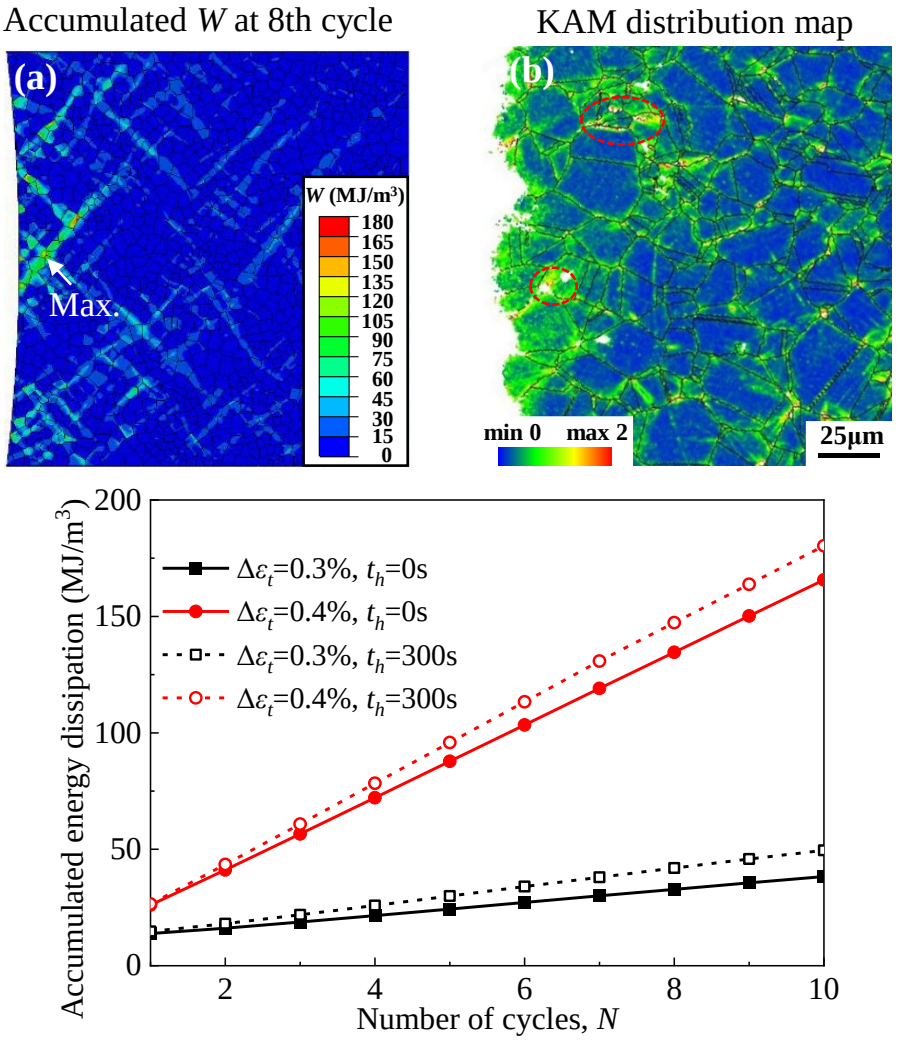

Figure 18 Damage evolutions from simulated results and experimental observation: (a) accumulated energy dissipation contour at 8th cycle and (b) KAM distribution map at holed root for specimen H8 under creep-fatigue loading condition with $\Delta\varepsilon_t$=0.4% and t_h =1800s; (c) the relation between accumulated energy dissipation and the number of cycles under different loading conditions.

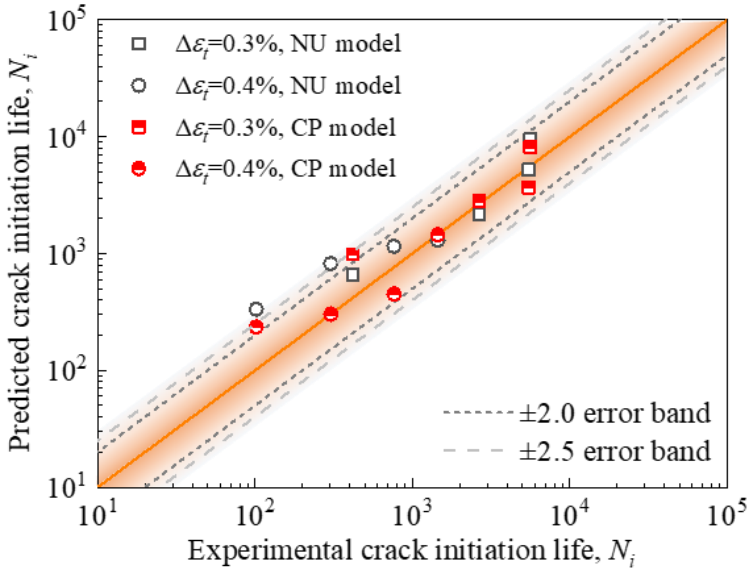

Figure 19 Comparisons between experimental creep-fatigue crack initiation life and predicted results based on NU model and CP model for holed specimens under different loading conditions in Inconel 718.

Table 1 Detailed parameters of the uniaxial round bar and central circular hole specimens in creep-fatigue tests for Inconel 718.

Waveform	Specimen	ID.	Temp.(°C)	R_ε	$\Delta\varepsilon_t$ (%)	t_h (s)
		U1	650	0	1.2	0
		U2	650	0	1.2	60
		U3	650	0	1.2	300
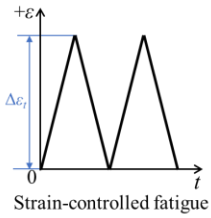	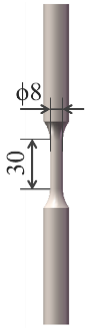	U4	650	0	1.6	0
		U5	650	0	1.6	60
		U6	650	0	1.6	300
		U7	650	0	1.6	1800
		U8	650	0	2.0	0
		U9	650	0	2.0	60
Strain-controlled fatigue		U10	650	0	2.0	300
		H1	650	0	0.3	0
		H2	650	0	0.3	60
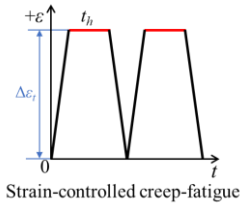	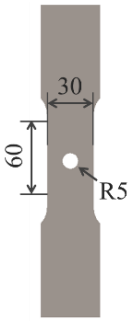	H3	650	0	0.3	300
		H4	650	0	0.3	1800
		H5	650	0	0.4	0
		H6	650	0	0.4	60
		H7	650	0	0.4	300
Strain-controlled creep-fatigue		H8	650	0	0.4	1800

Table 2 Material parameters of NU model for Inconel 718 at 650 ℃.

Category	Parameter	Unit	Value
Basic material constants	E	GPa	187
	ν	--	0.3
	Q_0	MPa	712
Kinematic hardening parameters	$\zeta^{(1)}$	--	428590
	$\zeta^{(2)}$	--	2425
	$\zeta^{(3)}$	--	11000
	$r^{(1)}$	--	50
	$r^{(2)}$	--	30
	$r^{(3)}$	--	1
Strain-hardening creep parameters	ψ	--	5.82×10^{-23}
	m	--	-0.68
	n	--	5.80
Isotropic hardening parameters	R_{sat}	MPa	-210
	b	--	2.6
Creep-fatigue damage parameters	m_f	--	2058910
	n_f	--	3.62
	m_c	--	115
	n_c	--	0.14
	w_{crit}	MJ/m^3	46

Table 3 Material parameters in CP model for Inconel 718 at 650 ℃.

Category	Parameter	Unit	Value
Anisotropic stiffness constants	C_{11}	GPa	205
	C_{12}	GPa	87
	C_{44}	GPa	64
Flow parameters	p	--	0.96
	q	--	1.12
	$\dot{\gamma}_0$	s^{-1}	120
	F_0	kJ/mol	295
	τ_0	MPa	485
Hardening parameters	h_B	MPa	850
	r_D	MPa	8
	r_S	s^{-1}	0.001
	h_S	MPa	360
	S_{sat}	MPa	317
	S_0	MPa	340
	w	--	1